The Dissertation Committee for Mikhail R. Tushentsov
certifies that this is the approved version of the following dissertation:

Numerical modeling of plasma detachment from a magnetic nozzle

Committee:

Roger Bengtson, Supervisor

Boris Breizman, Supervisor

Richard Hazeltine

Wendell Horton

Gary Hallock

Numerical modeling of plasma detachment from a magnetic nozzle

by

Mikhail R. Tushentsov, M.S.

DISSERTATION

Presented to the Faculty of the Graduate School of
The University of Texas at Austin
in Partial Fulfillment
of the Requirements
for the Degree of

DOCTOR OF PHILOSOPHY

THE UNIVERSITY OF TEXAS AT AUSTIN
December 2010

Acknowledgments

I gratefully acknowledge the guidance and contributions provided by my supervisors Boris Breizman and Roger Bengtson. Fruitful and inspiring discussions with them positively influenced my comprehension of the crucial moments of plasma physics. I also would like to thank my dissertation committee of Richard Hazeltine, Wendell Horton and Gary Hallock for their review and constructive suggestions that helped me to improve this document.

I would like to thank Ad Astra Rocket Company and its President and CEO Dr. Franklin Chang Díaz for financial support of this research. With gratitude I would also like to thank Elaine Kant, CEO and Curt Randall, Executive Vice President of Scicomp Inc. for their support and useful discussions.

I am indebted to my colleague and friend Alexey Arefiev who helped me greatly with various theoretical and numerical aspects of the project. In addition, I would like to thank Christoper Deline and Jackie Meyer for providing the experimental data. Furthermore, I express my thankfulness to all the staff of the Institute for Fusion Studies and the Department of Physics for creating an excellent work atmosphere and providing all necessary support.

Finally, I would like to thank my wife Irina, my son Stephen and my daughter Elizabeth for their gracious understanding, patience and inspiration during the thesis development. I am also heartily thankful to my parents Zoya and Rostislav, my sister Olga, my mother-in-law Larissa and my wife's grandparents Valentina and Vladimir for their encouragement and support.

Numerical modeling of plasma detachment from a magnetic nozzle

Publication No. ____________________

Mikhail R. Tushentsov, Ph.D.
The University of Texas at Austin, 2010

Supervisors: Roger Bengtson
Boris Breizman

The numerical simulation and modeling of plasma detachment from a magnetic nozzle is presented. The detachment problem is of key importance to the plasma-based propulsion concepts that employ a guiding magnetic field to control plasma flow and motivated by the needs of the VASIMR (Variable Specific Impulse Magnetoplasma Rocket) project. The detachment of the plasma exhaust is required to produce directed thrust. In the present scenario plasma can stretch the magnetic field lines to infinity, similar to the solar wind. In order to extend the magnetic nozzle model beyond the limitations of analytic theory, a numerical code is developed to simulate steady-state kinetic plasma flows and to evaluate nozzle efficiency. The direct solution of a steady-state problem, as opposed to an initial value problem, eliminates the need to deal with transient phenomena that are of secondary importance for continuously operated plasma thrusters. The new simulation code is verified against the analytic results and then used to model the plasma behaviour for the conditions of the Detachment Demonstration Experiment (DDEX) at the NASA Marshall Propulsion Research Center, Huntsville, Alabama.

Table of Contents

List of Tables

List of Figures

Chapter 1

Introduction

The exploration of space is one of the most important directions of human technological activity. It has expanded the horizon of scientific knowledge and lead to many direct and indirect benefits for mankind. The key element of successful space exploration is efficient and reliable propulsion technology. Since the beginning of the spaceflight era, the conventional chemical rocketry has been used to launch spacecrafts and correct their positions in orbit. While it works fine for the ground launch (and there is no real alternative) and orbital maneuvering, it has several limitations and drawbacks for the interplanetary travel. For the manned missions beyond Earth's orbit, a relevant spaceship must be fast and it should have reasonable abort options for crew safety. The travel time must be minimized in order to reduce the effects of the long space travel hazards like radiation, weightlessness and various psychological difficulties [39]. It is also desirable to have a thruster with low propellant consumption in order to cut down on propellant weight and increase useful payload.

1.1 Plasma-based propulsion concept

The above-mentioned requirements can be met by using devices with a continuous thrust such as high power plasma-based electric propulsion systems. A conventional chemical rocket accelerates in a short burst in the beginning of the journey and then follows a ballistic trajectory to the point of final destination. In contrast with this, a spacecraft with a continuous thrust would spend roughly half of the travel time accelerating and the other half slowing down. Such a spacecraft is not constrained to a ballistic trajectory, so that its trajectory can be optimized in order to decrease the travel time. It is essential that continuous thrust gives the option of aborting the mission and returning back from early in the flight. Plasma-based propulsion systems are not only capable of providing continuous thrust, but they also allow one to vary the exhaust velocity. A system with a variable velocity can handle both the cruise phase of the journey and the maneuvering near the origin and destination planets. This characteristic makes plasma-based systems even more attractive.

In the assumption of fixed exhaust velocity, the thrust developed by the rocket is equal to $T = (dM/dt)v_{ex}$ or in terms of specific impulse (change in momentum per unit amount of propellant used) $T = (dM/dt)g_0 I_{sp}$, where g_0 is the gravitational acceleration at the earths surface and dM/dt is the propellant consumption rate. Therefore, by increasing the specific impulse (or exhaust velocity), a propulsion system can be made more propellant-efficient without sacrificing the thrust level. While a standard chemical rocket (e.g. the space shuttle main engine) produces a maximum I_{sp} of 460 s [20], electric thrusters, such as the ion thrusters [28], can produce I_{sp} several orders of magnitude higher. Thus, larger payloads are possible since less propellant mass need be used for a given mission. (For example, Mars mission is required to carry 85% of its weight as fuel with conventional 300 s rocket, vs. 15% for a 3000 s I_{sp} electric propulsion thruster [27]).

In a chemical rocket, the exhaust velocity is related to the combustion temperature. This temperature is limited by the energy stored in the chemical bonds of the reactants, which does not exceed a few electron volts (eV).

A significant increase in the exhaust velocity would require at least 10 eV per particle. At these energies ionization occurs, so that one has to consider plasma as a propellant. The energy required to produce a single electron-ion pair considerably exceeds the ionization potential, because the ionization is unavoidably accompanied by excitation and atomic line radiation. The kinetic energy of ions in the exhaust should be significantly above the ionization potential, since only in this case the major part of the energy will go into ion acceleration rather than into plasma production. The most favorable energy range per particle for plasma-based propulsion systems is in a range of hundreds of electron volts.

A chemical rocket propellant consists of both a fuel and an oxidizer and it is simultaneously the source of energy and a working substance (its combustion products) for expending energy. In contrast, the plasma-based systems utilize the propellant only as a working substance and low propellant consumption is achieved through high energy consumption, where the energy is provided by a separate power supply.

The present power sources deployed in the space, such as solar arrays, can provide the levels of power in 10-100kW range [38] which is not enough for the full scale thruster capable of interplanetary missions. An energy source that can release more than a hundred electron volts per fuel particle is needed. Otherwise, the mass of the energy source alone is going to be higher than the propellant mass. The only way to achieve this level of energy density is through the nuclear reaction. For this reason, a fission nuclear reactor would be a relevant energy source for plasma-based thrusters. The liquid metal (lead-bismuth eutectic) cooled fast neutron reactors, which have relatively light and compact design, can be potentially deployed as an energy source providing the power output in the range of 10 - 100 MW [35].

1.2 Magnetic nozzle and detachment issue

An important feature of some high-power plasma thrusters is the presence of a strong guiding magnetic field forming a magnetic nozzle. The magnetic field directs the plasma flow axially, increasing its directed axial energy and preventing it from expanding radially towards the thruster walls. Some high powered plasma propulsion concepts employing a magnetic nozzle include applied-field MPD thrusters [33], fusion rockets, [21, 40] , the Variable Specific Impulse Magnetoplasma Rocket (VASIMR) [1, 30] and helicon thrusters [9, 34]. In particular, the VASIMR concept provides motivation for the present work due to its high power and high reliability. It has electrodeless design so that the thruster lifetime is not limited by the electrode erosion and the scaling to high power levels is possible.

The use of a strong magnetic field brings up the issue of plasma detachment from the magnetic nozzle [16, 25]. Plasma detachment process is different from the isolated charged particle detachment in the following way: A single ion will follow the magnetic field line trajectory if its gyroradius is much less than the characteristic spatial scale of the magnetic field (magnetized ion), but it can escape if it is no longer magnetized, i.e. the above condition is broken. However, for sufficiently dense plasma, ions can only escape together with electrons due to the plasma quasineutrality condition. The electrons have a much smaller gyroradius than the ions and can remain tied to magnetic field lines even when the ions are not magnetized, which makes it more difficult for ions to escape. One common concern is that the plasma flow may not be able to break-free from the thruster to produce thrust, because the field lines generated by the thruster magnets are closed. A failure to detach leads to inefficient propulsion due to highly divergent exhaust plasma flow. One of suggested approaches of how to solve this problem was breaking the frozen-in constraint via recombination [16]. Later it was shown [2, 19], that this issue can be resolved in the framework of ideal magnetohydrodynamics (MHD) and the efficient detachment is possible for a sufficiently long nozzle. The problem of a plasma flow in magnetic nozzles has received considerable attention in the past modeling efforts. This includes significant work associated with theta pinches and magnetoplasmadynamic (MPD) thrusters [32] [42]. A commonly accepted approach to such modeling is based on the MHD equations with either collision dominated or phenomenological transport coefficients. This approach implies a short mean free path for the plasma particles, which is typically not the case in the detachment problem because the plasma density decreases rapidly in the diverging nozzle.

The magnetic nozzle flow can be virtually divided into two regions, depending on the degree of influence of the applied magnetic field on the plasma flow. The criterion in this case is a ratio of the plasma flow kinetic energy density $\varepsilon_K = nMv^2/2$ to the magnetic energy density $\varepsilon_B = B^2/(8\pi)$ or plasma β (the more commonly used definition for plasma β uses the thermal energy). At the nozzle entrance, where the magnetic field reaches its maximum, the plasma β is small (much less than unity) and the magnetic field, due to the plasma currents, is negligible compare to the applied magnetic field. Therefore the plasma particle follows the field lines of the applied guiding magnetic field. In contrast, for the plasma nozzle exhaust region the plasma β is large due to the fact that the magnetic field energy density decreases more quickly than the directed kinetic energy density. This conclusion comes from the magnetic flux, plasma flow flux and ion kinetic energy conservation. For example, if one considers the uniform magnetic field and plasma density across the nozzle cross-section with the area S then the magnetic flux is BS and flow flux is $n_i u_{||} S$. Hence $\varepsilon_B \sim 1/S^2$ and $\varepsilon_K \sim 1/S$. Thus ε_B eventually becomes smaller than ε_K. Therefore the total magnetic field in the plasma is almost entirely due to the plasma currents. The magnetic field lines (total magnetic field) remain frozen into the plasma, as the flow stretches them to infinity (some amount of the magnetic flux is trapped along the plasma flow). In this case the plasma particle trajectories no longer follow the applied magnetic field lines. This is similar to what occurs in the solar wind as it moves away from the Sun [26].

The plasma β is directly related to the Alfvénic Mach number M_{A}, or the ratio of the plasma flow velocity to the Alfvén velocity v_{A}.

$$\beta = \frac{\varepsilon_K}{\varepsilon_B} = \frac{v^2}{v_{\mathrm{A}}^2} = \mathrm{M}_{\mathrm{A}}^2, \tag{1.1}$$

where $v_{\mathrm{A}} = B/\sqrt{4\pi n m_i}$ is the Alfvén velocity, m_i is the plasma ion mass, n and v plasma flow density and velocity correspondingly. The transition from low plasma β to high β is equivalent to flow acceleration from sub-Alfvénic to super-Alfvénic velocities and it is analogous to the de Laval nozzle in gas-dynamics with subsonic to supersonic transition.

In addition to the detachment, the other function of the magnetic nozzle is the conversion of the ion gyromotion energy to the directed flow energy. Under the assumption that the total ion kinetic energy $K = m\mathrm{v}^2/2$ and the ion magnetic moment $\mu = m\mathrm{v}_\perp^2/(2B)$ are conserved, the nozzle transforms the ion gyromotion into the axial motion, accelerating the plasma flow. In the case of VASIMR, the incoming plasma flow is produced by an ion cyclotron resonance heating (ICRH) module that deposits energy directly into ion gyromotion.

The objective of the present work is to generalize the detachment model of Ref. [2] to the case of kinetic ions and to develop a numerical code that could serve as a design tool to evaluate and optimize the nozzle efficiency. The kinetic treatment is necessary since the cold ion approximation in Ref. [2] is only applicable to the case of sufficiently small ion velocity spread. For example, the plasma flow entering the ICRH module of VASIMR typically has a significant spread in the ion axial velocities. This spread may translate into a spread in the ion gyroenergies depending on specific conditions of single-pass ICRH scheme [1, 7].

In Chapter 2 the set of basic equations for the steady-state paraxial flow in magnetic nozzle is formulated. In Chapter 3 the numerical procedure description is presented. In Chapter 4 the numerical code is benchmarked against the analytical solution for flow in the conical nozzle with rarefaction wave at the edge of the plasma plume. It is followed by more plasma flow simulations for the cases that are not analytically treatable and, finally, the model of the plasma plume in a recent Detachment Demonstration Experiment (DDEX) at the NASA Marshall Space Flight Center [3, 10] is presented.

The key results of the thesis were published in Refs. [6, 12] and presented at the following conferences: 49th Annual Meeting of the Division of Plasma Physics of the American Physical Society and 2007 Sherwood Fusion Theory Conference.

Chapter 2

Magnetic Nozzle Model Formulation

The magnetic nozzle consists of the plasma flow and the surrounding vacuum region with a guiding magnetic field generated by the system of current coils. It is convenient to solve the problem in the plasma and vacuum separately and then match the solutions at the plasma-vacuum interface using the proper boundary conditions. This approach is motivated by the fact that it is hard to solve the plasma equations in the regions with very low (zero) density which formally leads to infinite Alfvén velocities. Therefore we formulate two sets of governing equations describing the plasma and the vacuum region with external current sources.

2.1 Governing equations for the steady-state plasma flow

We start with Vlasov-Maxwell equations for collisionless plasma. We consider a preformed steady-state supersonic plasma flow that consists of energetic ions and cold electrons. When the flow is strongly supersonic, the electron pressure is naturally less important than the dynamic pressure of ions, and the same argument applies to the ambipolar electric field. It should be noted that the electric field is nevertheless important during transition stage from sub- to supersonic flow which is direct consequence of the ambipolar acceleration. The high electron conductivity along the magnetic field lines results in the absence of the parallel electric field. Considering the incoming plasma flow without macroscopic rotation, or equivalently without an $\mathbf{E} \times \mathbf{B}$ drift, we neglect the transverse component (with respect to magnetic field) of the electric field.

The resulting steady-state Vlasov equation for the ion distribution function f_i has the form:

$$m_i \mathbf{v} \cdot \nabla f_i + \frac{q_i}{c} [\mathbf{v} \times \mathbf{B}] \cdot \nabla_{\mathrm{v}} f_i = 0. \tag{2.1}$$

The Vlasov equation for cold electrons with zero inertia is

$$\frac{q_e}{c} [\mathbf{v} \times \mathbf{B}] \cdot \nabla_{\mathrm{v}} f_e = 0. \tag{2.2}$$

The Maxwell equations require that the magnetic field $\mathbf{B}$ is divergence-free,

$$\nabla \cdot \mathbf{B} = 0, \tag{2.3}$$

and that the field is related to the plasma current by the Ampère's law:

$$\nabla \times \mathbf{B} = \frac{4\pi}{c} \left(q_i \int \mathbf{v} f_i d^3\mathrm{v} + q_e \int \mathbf{v} f_e d^3\mathrm{v} \right). \tag{2.4}$$

where $q_i = Ze$ and $q_e = -e$ are the ion and electron charge correspondingly, Z is the ion charge number.

Equations (2.1) - (2.4) conserve mass and momentum. Using the general transport equation technique for the averaged macroscopic properties [4], we can write the following conservation relations:

$$\nabla \cdot \left(m_i \int f_i \mathbf{v} d^3\mathrm{v} \right) = 0, \tag{2.5}$$

$$\nabla \cdot \left(m_e \int f_e \mathbf{v} d^3\mathrm{v} \right) = 0, \tag{2.6}$$

$$\nabla \cdot \left(m_i \int f_i \mathbf{v}\mathbf{v} d^3\mathrm{v} \right) + \mathbf{B} \times \frac{q_i}{c} \int f_i \mathbf{v} d^3\mathrm{v} = 0, \tag{2.7}$$

$$\mathbf{B} \times \frac{q_e}{c} \int f_e \mathbf{v} d^3\mathrm{v} = 0. \tag{2.8}$$

We find from Eq. (2.8) that the cold electrons have no macroscopic velocity (carry no current) across the magnetic field. The cross-field current is then carried only by ions, so that

$$\mathbf{j}_\perp = q_i \int f_i \mathbf{v}_\perp d^3\mathrm{v}. \tag{2.9}$$

Combining the Eq. (2.4), Eq. (2.7) and Eq. (2.8) we obtain:

$$\nabla \cdot \left(m_i \int f_i \mathbf{v}\mathbf{v} d^3\mathrm{v} \right) + \frac{1}{4\pi} \mathbf{B} \times [\nabla \times \mathbf{B}] = 0. \tag{2.10}$$

Taking into account the Eq. (2.3) we come to the the following momentum balance equation for the ions:

$$\nabla \cdot \left(\mathbf{\Pi} + \frac{|\mathbf{B}|^2}{8\pi} \mathbf{I} - \frac{\mathbf{B}\mathbf{B}}{4\pi} \right) = 0, \tag{2.11}$$

where

$$\mathbf{\Pi} \equiv m_i \int \mathbf{v}\mathbf{v} f_i d^3\mathrm{v} \tag{2.12}$$

is the ion momentum flux tensor that includes both the flux associated with the directed flow and the flux associated with the ion velocity spread (ion pressure).

The concept of a magnetic nozzle implies that the applied magnetic field is sufficiently strong to hold ions (and electrons) in orbits around the magnetic field lines (guiding center theory [29]). The ion velocity vector can be represented as

$$\mathbf{v} = \mathrm{v}_\perp \cos\psi \mathbf{x}_b + \mathrm{v}_\perp \sin\psi \mathbf{y}_b + \mathrm{v}_{||} \mathbf{b} \tag{2.13}$$

in the local cylindrical coordinate system at the given location on the magnetic field line, where $\mathbf{b}$ is the unit vector in the direction of the local magnetic field, $\mathbf{x}_b$, $\mathbf{y}_b$ are unit coordinate vectors in the plane perpendicular to the local magnetic field and ψ is the gyroangle in the velocity space.

Assuming that the ions are magnetized, so that their Larmor radii remain much smaller than the plasma radius, the ion distribution function can be viewed as independent of the gyroangle in the velocity space. Under this assumption the non-diagonal elements of the ion momentum flux tensor vanish and the diagonal elements can be written using a gyroaveraged distribution function defined as

$$\langle f_i \rangle \equiv \frac{1}{2\pi} \int_0^{2\pi} f_i \; d\psi. \tag{2.14}$$

In this limit, we have

$$\mathbf{\Pi} = \Pi_\perp \mathbf{I} + \left(\Pi_\| - \Pi_\perp \right) \mathbf{bb}, \tag{2.15}$$

where $\mathbf{I}$ is the identity tensor

$$\mathbf{I} = \mathbf{x}_b \mathbf{x}_b + \mathbf{y}_b \mathbf{y}_b + \mathbf{bb}, \tag{2.16}$$

and the ion momentum flux tensor components are

$$\Pi_\perp \equiv \frac{m_i}{2} \int \mathrm{v}_\perp^2 \, \langle f_i \rangle \, d^3\mathrm{v}, \tag{2.17}$$

$$\Pi_\| \equiv m_i \int \mathrm{v}_\|^2 \, \langle f_i \rangle \, d^3\mathrm{v}, \tag{2.18}$$

where $d^3\mathrm{v} = 2\pi \mathrm{v}_\perp \mathrm{dv}_\perp \mathrm{dv}_{||}$. It should be noted that the local coordinate system in the velocity space implies the space dependence of the velocity components. The ion magnetic moment

$$\mu = m_i \mathrm{v}_\perp^2 / 2B \tag{2.19}$$

and the ion energy

$$\varepsilon \equiv m_i \left(\mathrm{v}_\perp^2 + \mathrm{v}_{||}^2 \right)/2 \tag{2.20}$$

are invariants in the guiding center motion therefore they are constant along the magnetic field lines

$$(\mathbf{b} \cdot \nabla)\, \mu = 0, \qquad (\mathbf{b} \cdot \nabla)\, \varepsilon = 0. \tag{2.21}$$

Changing the integration variables in expressions (2.17) and (2.18) from $\mathrm{v}_\perp$ and $\mathrm{v}_{||}$ to ε and μ, i.e.,

$$d^3\mathrm{v} = \pi d\mathrm{v}_\perp^2 d\mathrm{v}_{||} = \frac{\pi}{2} \left(\frac{2}{m_i} \right)^{\frac{3}{2}} \frac{B}{\sqrt{\varepsilon - \mu B}} d\mu d\varepsilon, \tag{2.22}$$

we can obtain the following expressions for $\Pi_{||}$ and $\Pi_\perp$ as functionals of the magnetic field:

$$\Pi_\perp[B] = \frac{\pi}{2} \left(\frac{2}{m_i} \right)^{\frac{3}{2}} \int B \frac{\mu B}{\sqrt{\varepsilon - \mu B}} \left\langle f_i \right\rangle \ \mathrm{d}\mu \mathrm{d}\varepsilon, \tag{2.23}$$

$$\Pi_{||}[B] = \pi \left(\frac{2}{m_i} \right)^{\frac{3}{2}} \int B \sqrt{\varepsilon - \mu B} \left\langle f_i \right\rangle \ \mathrm{d}\mu \mathrm{d}\varepsilon. \tag{2.24}$$

Taking the projection along the magnetic field line for the Eq. (2.7) we can write the following relation for the ion momentum flux tensor:

$$\mathbf{b} \cdot (\nabla \cdot \mathbf{\Pi}) = 0. \tag{2.25}$$

Substituting the tensor components $\Pi_{||}$ and $\Pi_\perp$ we have

$$(\mathbf{b} \cdot \nabla)\, \Pi_{||} + \left(\Pi_{||} - \Pi_\perp \right) (\nabla \cdot \mathbf{b}) = 0. \tag{2.26}$$

The Eq. (2.26) can be rewritten in terms of derivatives along the magnetic field lines only (Appendix A), using the Eq. (2.3) expressed through the magnetic unit vector $\mathbf{b} = \mathbf{B}/|\mathbf{B}|$ and the magnetic field magnitude $B = |\mathbf{B}|$ which has the following form

$$(\mathbf{b} \cdot \nabla) B + B \nabla \cdot \mathbf{b} = 0. \tag{2.27}$$

Hence we get

$$(\mathbf{b} \cdot \nabla) \left(\frac{\Pi_{||}}{B} \right) + \frac{\Pi_{\perp}}{B^2} (\mathbf{b} \cdot \nabla) B = 0. \tag{2.28}$$

Replacing the $\Pi_{\perp}$ and $\Pi_{||}$ with their functional forms (2.24) and (2.23) in Eq. (2.28) we obtain

$$\int \sqrt{\varepsilon - \mu B} \; (\mathbf{b} \cdot \nabla) \langle f_i \rangle \; \mathrm{d}\mu \mathrm{d}\varepsilon = 0. \tag{2.29}$$

Therefore, the gyroaveraged distribution function is constant along the magnetic field lines, i.e.

$$m_i v_{||} (\mathbf{b} \cdot \nabla) \langle f_i \rangle = 0. \tag{2.30}$$

Eq. (2.30) is a version of the drift-kinetic equation [18]. Eq. (2.30) can be also viewed as gyroaveraged stationary Vlasov equation known from the lowest order guiding center theory. Eq. (2.30) can be directly obtained by the integration of the Eq. (2.1) over the gyroangle and using the assumption about the small Larmor radius. This lowest order solution $\langle f_i \rangle$ is apparently independent of gyrophase. As a result, it does not contribute to the ion current defined by Eq. (2.9). The ion current is determined by the small gyrophase-dependent corrections to the distribution function, associated with the curvature drift and the diamagnetic drift. These small current-carrying corrections can be safely neglected in expressions (2.17) and (2.18) for the momentum flux tensor.

Dropping the tensor notation in the Eq. (2.11) we obtain

$$\nabla \left(\Pi_{\perp} + \frac{B^2}{8\pi} \right) + (\mathbf{b} (\mathbf{b} \cdot \nabla) + (\mathbf{b} \cdot \nabla) \mathbf{b}) \left(\Pi_{||} - \Pi_{\perp} - \frac{B^2}{4\pi} \right) = 0. \tag{2.31}$$

Using Eq. (2.26) and (2.27) we rewrite the Eq. (2.31) in the following form

$$(\nabla - \mathbf{b}\,(\mathbf{b}\cdot\nabla))\left(\Pi_\perp + \frac{B^2}{8\pi}\right) + \left(\Pi_\parallel - \Pi_\perp - \frac{B^2}{4\pi}\right)(\mathbf{b}\cdot\nabla)\,\mathbf{b} = 0. \qquad (2.32)$$

where the first term contains the derivative normal to the field lines. The Eqs. (2.32) and (2.27) along with the conservation equations Eqs. (2.21) and (2.30) (subject to appropriate boundary conditions) determine the self-consistent configuration of the magnetic field in the plasma flow.

2.2 Paraxial approximation

The above described model can be tailored to the case of most practical interest, a nozzle that produces a well-directed plasma flow. The latter implies that the radial component of the magnetic field in the plasma is much smaller than the axial component of the field. It also implies that the plasma flow is highly super-Alfvénic at the nozzle exit. Violation of any of these two conditions will clearly degrade the nozzle efficiency. Our goal then is to ensure that the model is sufficiently accurate in the regimes where both conditions are satisfied. This will allow us to quantify the nozzle efficiency in the most relevant parameter range. The model will be less accurate at low efficiencies, but these regimes are of little interest anyway. Yet, even without being quantitative with regard to inefficient nozzles, the model can still serve as an indicator of what parameter range to avoid.

Guided by these thoughts, we simplify Eq. (2.32) by neglecting the term $(\Pi_\perp + B^2/4\pi)\,(\mathbf{b}\cdot\nabla)\,\mathbf{b}$ compared to $(\nabla - \mathbf{b}\,(\mathbf{b}\cdot\nabla))\,(\Pi_\perp + B^2/8\pi)$, as we assume that the radial spatial scale is much shorter than the axial scale in a well-directed flow. We still keep the term $\Pi_\parallel\,(\mathbf{b}\cdot\nabla)\,\mathbf{b}$ in this equation because the parallel component of the momentum flux tensor exceeds $B^2/8\pi$

in a highly super-Alfvénic flow. Moreover, the term $\Pi_{||}\left(\mathbf{b}\cdot\nabla\right)\mathbf{b}$ eventually becomes the dominant one in Eq. (2.32) as both the magnetic pressure and $\Pi_{\perp}$ decrease downstream faster than $\Pi_{||}$. The fast decrease of $\Pi_{\perp}$ results from the conservation of magnetic moment for magnetized ions. Considering the axisymmetric geometry of the system, the magnetic field therefore has only two components (axial and radial) $\mathbf{b} = (B_r/B)\mathbf{e}_r + (B_z/B)\mathbf{e}_z$. The corresponding plasma current has only one (azimuthal) component (transverse to the (r, z) plane of the cylindrical coordinate system). In this case an additional relevant approximation is to replace B^2 by B_z^2 in all expressions, because the radial component of the magnetic field gives only a second order correction to B^2 in our problem of interest.

As a result of the described approximations, we finally obtain the following simplified set of basic equations in cylindrical coordinates:

$$\left(\frac{\partial}{\partial z}+\frac{B_r}{B_z}\frac{\partial}{\partial r}\right)B_z=-B_z\frac{1}{r}\frac{\partial}{\partial r}\left(r\frac{B_r}{B_z}\right), \tag{2.33}$$

$$\left(\frac{\partial}{\partial z}+\frac{B_r}{B_z}\frac{\partial}{\partial r}\right)\frac{B_r}{B_z}=-\frac{1}{\Pi_{||}}\frac{\partial}{\partial r}\left(\Pi_{\perp}+\frac{B_z^2}{8\pi}\right), \tag{2.34}$$

where the parallel and transverse pressure tensor components are:

$$\Pi_{||}[B_z]=\pi\left(\frac{2}{m_i}\right)^{\frac{3}{2}}\int B_z\sqrt{\varepsilon-\mu B_z}\,\langle f_i\rangle\;\mathrm{d}\mu\mathrm{d}\varepsilon, \tag{2.35}$$

$$\Pi_{\perp}[B_z]=\frac{\pi}{2}\left(\frac{2}{m_i}\right)^{\frac{3}{2}}\int B_z\frac{\mu B_z}{\sqrt{\varepsilon-\mu B_z}}\,\langle f_i\rangle\;\mathrm{d}\mu\mathrm{d}\varepsilon. \tag{2.36}$$

The ion distribution function $\langle f_i\rangle$, the ion magnetic moment μ, the ion kinetic energy ε and the magnetic flux function Φ are conserved along the field lines:

$$\left(\frac{\partial}{\partial z}+\frac{B_r}{B_z}\frac{\partial}{\partial r}\right)X=0, \tag{2.37}$$

where $X = \langle f_i \rangle, \mu, \varepsilon, \Phi$ and the magnetic flux function is:

$$\Phi(r,z) = 2\pi \int_0^r B_z(r',z) r' dr'. \tag{2.38}$$

Hence the ion distribution function is the function of Φ, μ, ε only:

$$\langle f_i \rangle = F(\Phi, \mu, \varepsilon). \tag{2.39}$$

The plasma flow characteristics, the ion density and the ion current density, have the following expressions:

$$n_i = B_z \frac{\pi}{2} \left(\frac{2}{m_i}\right)^{\frac{3}{2}} \iint\limits_{\varepsilon > \mu B_z} \langle f_i \rangle (\Phi, \mu, \varepsilon) \frac{1}{\sqrt{\varepsilon - \mu B_z}} d\mu d\varepsilon, \tag{2.40}$$

$$J_i = ZeB_z \frac{\pi}{2} \left(\frac{2}{m_i}\right)^2 \iint\limits_{\varepsilon > \mu B_z} \langle f_i \rangle (\Phi, \mu, \varepsilon) d\mu d\varepsilon. \tag{2.41}$$

From Eq. (2.41) we can derive that the quantity J_i/B_z is conserved along the magnetic field lines, i.e.

$$\left(\frac{\partial}{\partial z} + \frac{B_r}{B_z}\frac{\partial}{\partial r}\right)\left(\frac{J_i}{B_z}\right) = 0, \tag{2.42}$$

which is a consequence of the ion mass flux and magnetic flux conservation.

Let us now consider some simple plasma flow configurations which are governed by the system (2.33) and (2.34). The simplest incoming flow with an axially symmetric magnetic configuration is the cylindrical flow. In this case the magnetic field lines are parallel to the axis (radial magnetic field is zero):

$$\left(\frac{B_r}{B_z}\right) = 0. \tag{2.43}$$

Hence, from Eq. (2.33) follows that $\partial B_z/\partial z = 0$ and (2.34)

$$\frac{\partial}{\partial r}\left(\Pi_\perp + \frac{B_z^2}{8\pi}\right) = 0, \tag{2.44}$$

i.e. total pressure is radially uniform.

Another simple flow is a conical flow where the magnetic field lines are straight and converge at a single point on the axis of the system. In this case:

$$\frac{B_r}{B_z} = \frac{r}{z}. \tag{2.45}$$

The equation for B_z becomes:

$$\left(\frac{\partial}{\partial z} + \frac{r}{z}\frac{\partial}{\partial r}\right)\left(r^2 B_z\right) = 0. \tag{2.46}$$

The total pressure in this flow is radially uniform as in the cylindrical flow case, as follows from (2.34). In the case of zero transverse ion kinetic energy we have a radially uniform axial magnetic field profile, i.e. $\partial B_z/\partial r = 0$. From (2.46) we then obtain:

$$B_(r, z) = B_z(r, z_0)\frac{z_0^2}{z^2}, \tag{2.47}$$

where z_0 is some axial position with known radial profile of axial magnetic field B_z.

2.3 No ion magnetic moment spread limit

Equations (2.33)-(2.34) reduce to paraxial ideal MHD equations with anisotropic pressure if all ions on a given magnetic flux surface have the same energy ε_* and the same magnetic moment μ_*, so the ion distribution function has the following form:

$$\langle f_i \rangle = F(\Phi)\delta\left(\mu - \mu_*\right)\delta\left(\varepsilon - \varepsilon_*\right). \tag{2.48}$$

In this case the expressions for the ion density and current become:

$$n_i = B_z \frac{\pi}{2}\left(\frac{2}{m_i}\right)^{\frac{3}{2}} \frac{F(\Phi)}{\sqrt{\varepsilon_* - \mu_* B_z}}, \tag{2.49}$$

$$J_i = ZeB_z \frac{\pi}{2} \left(\frac{2}{m_i} \right)^2 F(\Phi). \tag{2.50}$$

Therefore the directed flow velocity $u_\| = J_i/(Zen_i)$ can be written as:

$$u_\| = \left(\frac{2}{m_i} \right)^{\frac{1}{2}} \sqrt{\varepsilon_* - \mu_* B_z}. \tag{2.51}$$

Hence the ion momentum tensor components can be expressed as:

$$\Pi_{||} = 2n_i u_\|^2, \tag{2.52}$$

$$\Pi_\perp = n_i \mu_* B_z. \tag{2.53}$$

Taking into account expressions (2.52) and (2.53), we transform Eq. (2.34) into:

$$\left(\frac{\partial}{\partial z} + \frac{B_r}{B_z} \frac{\partial}{\partial r} \right) \frac{B_r}{B_z} = -\frac{1}{2n_i u_\|^2} \frac{\partial}{\partial r} \left(n_i \mu_* B_z + \frac{B_z^2}{8\pi} \right). \tag{2.54}$$

Equations (2.33) and (2.54) determine the self-consistent configuration of a paraxial magnetic field in the plasma flow. In the absence of gyromotion ($\mu_* = 0$), this set of equations is equivalent to the paraxial MHD description presented in Ref. [2].

The Eq.(2.42) becomes:

$$\left(\frac{\partial}{\partial z} + \frac{B_r}{B_z} \frac{\partial}{\partial r} \right) \left(\frac{n_i u_\|}{B_z} \right) = 0. \tag{2.55}$$

In the case without gyromotion $u_\| = \varepsilon_*$ therefore:

$$\left(\frac{\partial}{\partial z} + \frac{B_r}{B_z} \frac{\partial}{\partial r} \right) u_{||} = 0, \tag{2.56}$$

and

$$\left(\frac{\partial}{\partial z} + \frac{B_r}{B_z} \frac{\partial}{\partial r} \right) \left(\frac{n_i}{B_z} \right) = 0. \tag{2.57}$$

The Eqs. (2.56), (2.57) offer the simple way to calculate the flow density and velocity profiles in the nozzle region where the plasma currents do not significantly distort the external field configuration.

2.4 Magnetic field outside the plasma

As already pointed out, our goal is to simulate a well directed plasma flow, which implies that the field lines in the plasma are paraxial (both inside the nozzle and in the outgoing plasma plume). This regime requires the guiding magnetic field generated by the external coils to be paraxial inside the nozzle. However, the field lines are not necessarily paraxial in the vacuum region outside the plasma plume. This vacuum magnetic field is essential to our problem because it determines the boundary condition at the plasma-vacuum interface. The location of the plasma boundary needs to be found self-consistently, which couples the equations for magnetic field in the plasma to the equations for the vacuum field.

The stability of the plasma-vacuum interface implies the total pressure balance since without it the plasma would expand radially.

$$\left(\Pi_\perp + \frac{B_z^2}{8\pi}\right)_{r=r_{pv}} = \left(\frac{\left(B_z^{(v)}\right)^2}{8\pi}\right)_{r=r_{pv}}, \tag{2.58}$$

where $B_z^{(v)}$ is the vacuum magnetic field and $r = r_{pv}(z)$ is the curve that determines the plasma-vacuum interface position.

In order to find the vacuum magnetic field let us consider a magnetostatic problem for the magnetic field from the system of coils in presence of plasma flow in axisymmetric geometry. The equation for the magnetic vector potential ($\mathbf{B} = \nabla \times \mathbf{A}$) can be written as:

$$\nabla^2 \mathbf{A} = -\frac{4\pi}{c}\mathbf{J}, \tag{2.59}$$

where $\nabla^2 \mathbf{A}$ is the vector Laplacian and the Coulomb gauge $\nabla \cdot \mathbf{A} = 0$ is used. The current source is the axially symmetric system of coils. Therefore the current has only azimuthal component. In cylindrical coordinate system we can write the following equation:

$$\frac{1}{r}\frac{\partial}{\partial r}\left(r\frac{\partial A}{\partial r}\right)+\frac{\partial^2 A}{\partial z^2}-\frac{1}{r^2}A=-\frac{4\pi}{c}J, \tag{2.60}$$

where $\mathbf{A} = A(r,z)\mathbf{e}_\phi$, $\mathbf{J} = J(r,z)\mathbf{e}_\phi$ and $\mathbf{e}_\phi$ is the azimuthal unit vector. The magnetic field components can be found as:

$$B_r^{(v)} = -\frac{\partial A}{\partial z}, \tag{2.61}$$

$$B_z^{(v)} = \frac{1}{r}\frac{\partial}{\partial r}\left(rA\right). \tag{2.62}$$

Since, under our assumptions, the magnetic field lines are frozen into the plasma, they can not cross the boundary and are therefore tangential to it. Hence we have the normal component of the magnetic file vanishing at the plasma-vacuum interface:

$$\left(\mathbf{n}_{pv}\cdot\mathbf{B}^{(v)}\right)_{r=r_{pv}} = 0, \tag{2.63}$$

where $\mathbf{n}_{pv}$ is the unit vector normal to the boundary (defined by the parametric curve $r = r_{pv}(z)$). This condition can be expressed through the magnetic field components as:

$$\left(\frac{B_r^{(v)}}{B_z^{(v)}}\right)_{r=r_{pv}} = \frac{dr_{pv}}{dz}. \tag{2.64}$$

The vacuum magnetic field problem has analytical solution in case of cylindrical plasma flow and can be represented as a superposition of the magnetic fields from the system of coils encircling an ideally conducting rod with cylindrical cross section. The solution can be obtained from the variable separation in cylindrical coordinates and can be presented in the form of integral over the combination of the modified Bessel functions (Appendix B).

Chapter 3

Numerical scheme details

Once the model equations along with the corresponding boundary conditions are formulated, the next important step is to choose the appropriate numerical technique to solve the problem. As it is mentioned in the Chapter 2, the problem is split into the plasma and vacuum domains which are computed separately and the solutions are matched at the plasma-vacuum interface using the boundary conditions. Since the position of the plasma-vacuum boundary is not known a priori, an iterative procedure is required to determine it. The initial step is to calculate the vacuum magnetic field for a given configuration of the external coils with cylindrical plasma flow with radius r_p. Hence the magnetic field at the plasma-vacuum interface to the lowest order can be found. The next step now is to solve the plasma equations using this magnetic field as a boundary condition. This solution gives us the magnetic field in the plasma together with a corrected location of the plasma boundary $r = r_{pv}(z)$. The initial step presents a good approximation for the vacuum magnetic field outside a slowly diverging flow. The knowledge of the plasma boundary allows us to continue iterations. The described iterative procedure can be continued to achieve desired precision.

3.1 Numerical implementation of the plasma equations

The simulation of the plasma equations (2.33), (2.34) employ a Lagrangian grid associated with magnetic flux surfaces in the plasma. An important advantage of this grid is that it makes it particularly easy to trace the plasma-vacuum interface and to implement the corresponding boundary condition [42]. This grid is also convenient because the plasma radius increases considerably downstream from the nozzle exit.

The magnetic field components can be expressed using the magnetic flux function Φ defined in Eq. (2.38) as follows:

$$B_z = \frac{1}{2\pi r}\frac{\partial \Phi}{\partial r}, \tag{3.1}$$

$$B_r = -\frac{1}{2\pi r}\frac{\partial \Phi}{\partial z}. \tag{3.2}$$

The magnetic flux function Φ labels the magnetic flux surface (or magnetic field line surface, Appendix A) and therefore can be used as a new coordinate. The transformation Jacobian elements are:

$$\frac{\partial \Phi}{\partial r} = 2\pi r B_z, \qquad \frac{\partial \Phi}{\partial z} = -2\pi r B_z \frac{B_r}{B_z}, \tag{3.3}$$

$$\frac{\partial \tilde{z}}{\partial r} = 0, \qquad \frac{\partial \tilde{z}}{\partial z} = 1. \tag{3.4}$$

The partial derivatives in new coordinates are:

$$\frac{\partial}{\partial r} = 2\pi r B_z \frac{\partial}{\partial \Phi}, \tag{3.5}$$

$$\frac{\partial}{\partial z} + \frac{B_r}{B_z}\frac{\partial}{\partial r} = \frac{\partial}{\partial \tilde{z}}. \tag{3.6}$$

Switching from (r, z) to new variables $(\Phi, \tilde{z})$ in equations (2.33), (2.34), one can obtain the following system of equations (due to trivial transform for

z we can omit tilde notation for it):

$$\left(\frac{\partial r}{\partial z}\right)_\Phi = \frac{B_r}{B_z}, \tag{3.7}$$

$$\left[\frac{\partial}{\partial z}\left(\frac{B_r}{B_z}\right)\right]_\Phi = -\frac{1}{\Pi_\parallel} 2\pi r B_z \left[\frac{\partial}{\partial \Phi}\left(\Pi_\perp + \frac{B_z^2}{8\pi}\right)\right]_z. \tag{3.8}$$

In the assumption that the radius corresponds to the position of the magnetic fluid elements the following expression for the axial magnetic field B_z can be written using Eq. (3.1):

$$B_z = \frac{1}{\pi}\left(\frac{\partial r^2}{\partial \Phi}\right)_z^{-1}. \tag{3.9}$$

Equations (3.7) - (3.8) have the structure of one-dimensional evolution equations for the unknown functions r and B_r/B_z. We thereby reduce our steady-state problem to an initial value problem for Eqs. (3.7) - (3.8), with the coordinate z playing the role of time.

The computation domain in z-direction is bounded by magnetic nozzle entrance (incoming flow entry point) z_0 and the position far from the nozzle entrance z_∞, where the exhaust is fully formed. The initial conditions are set at $z = z_0$ as $B_{z0} = B_z(\Phi, z_0)$ and $(B_r/B_z)_0 = (B_r/B_z)(\Phi, z_0)$. If the incoming flow ion density profile $n_{i0} = n_i(\Phi, z_0)$ is given at z_0 instead of B_{z0} then the B_{z0} can be found from the incoming flow configuration information. It is convenient to rewrite all expressions that depend on the distribution function in the form which is independent of its normalization. Using the ion density n_{i0} and axial magnetic field B_{z0} profiles one can write the following expressions:

$$n_i = n_{i0}\frac{B_z}{B_{z0}} \iint\limits_{\varepsilon > \mu B_z} \langle f_i \rangle \left[\varepsilon - \mu B_{z0}\frac{B_z}{B_{z0}}\right]^{-\frac{1}{2}} d\mu d\varepsilon \left[\iint\limits_{\varepsilon > \mu B_{z0}} \frac{\langle f_i \rangle}{\sqrt{\varepsilon - \mu B_{z0}}} d\mu d\varepsilon\right]^{-1}, \tag{3.10}$$

$$\Pi_{||} = 2n_{i0}\frac{B_z}{B_{z0}}\iint\limits_{\varepsilon>\mu B_z}\langle f_i\rangle\left[\varepsilon-\mu B_{z0}\frac{B_z}{B_{z0}}\right]^{\frac{1}{2}}d\mu d\varepsilon\left[\iint\limits_{\varepsilon>\mu B_{z0}}\frac{\langle f_i\rangle}{\sqrt{\varepsilon-\mu B_{z0}}}d\mu d\varepsilon\right]^{-1}, \tag{3.11}$$

$$\Pi_{\perp} = n_{i0}\left(\frac{B_z}{B_{z0}}\right)^2\iint\limits_{\varepsilon>\mu B_z}\langle f_i\rangle\frac{\mu B_{z0}}{\sqrt{\varepsilon-\mu B_{z0}\frac{B_z}{B_{z0}}}}d\mu d\varepsilon\left[\iint\limits_{\varepsilon>\mu B_{z0}}\frac{\langle f_i\rangle}{\sqrt{\varepsilon-\mu B_{z0}}}d\mu d\varepsilon\right]^{-1}. \tag{3.12}$$

Let us consider the special class of distribution functions where the spatial dependence is separated from the energy dependence:

$$\langle f_i\rangle = F(\varepsilon-\mu B_{z0},\mu B_{z0})G(\Phi), \tag{3.13}$$

where $F(\varepsilon_{||},\varepsilon_{\perp})$ is the energy distribution function. (In the experiment the ion velocity distribution function can be determined, for example, by Laser Induced Fluorescence (LIF) technique [31]). In this case we can create the following lookup tables to speedup the frequent double integrals evaluation:

$$I_n(b) = \iint F(\varepsilon_{||},\varepsilon_{\perp})\frac{1}{\sqrt{\varepsilon_{||}+\varepsilon_{\perp}(1-b)}}\mathrm{d}\varepsilon_{\perp}\mathrm{d}\varepsilon_{||}, \tag{3.14}$$

$$I_{||}(b) = \iint F(\varepsilon_{||},\varepsilon_{\perp})\sqrt{\varepsilon_{||}+\varepsilon_{\perp}(1-b)}\,\mathrm{d}\varepsilon_{\perp}\mathrm{d}\varepsilon_{||}, \tag{3.15}$$

$$I_{\perp}(b) = \iint F(\varepsilon_{||},\varepsilon_{\perp})\frac{\varepsilon_{\perp}}{\sqrt{\varepsilon_{||}+\varepsilon_{\perp}(1-b)}}\mathrm{d}\varepsilon_{\perp}\mathrm{d}\varepsilon_{||}, \tag{3.16}$$

where $b \in [0,1]$, $\varepsilon_{\perp} = \mu B_{z0}$, $\varepsilon_{||} = \varepsilon - \mu B_{z0}$. Using the above tabulated functions the following expressions can be written:

$$\Pi_{||} = 2n_{i0}\frac{B_z}{B_{z0}}I_{||}\left(\frac{B_z}{B_{z0}}\right)/I_n(1), \tag{3.17}$$

$$\Pi_{\perp} = n_{i0}\left(\frac{B_z}{B_{z0}}\right)^2 I_{\perp}\left(\frac{B_z}{B_{z0}}\right)/I_n(1), \tag{3.18}$$

$$n_i = n_{i0} \frac{B_z}{B_{z0}} I_n \left(\frac{B_z}{B_{z0}} \right) / I_n(1). \tag{3.19}$$

Now one can compute the initial condition for the axial field B_{z0} as:

$$B_{z0} = \sqrt{B_{zv}^2(z_0) - 8\pi n_{i0} I_\perp(1)/I_n(1)}. \tag{3.20}$$

In the radial direction we form a staggered grid [36] for magnetic flux surface radii at the entrance position, $(r_0)_j, (r_0)_{j+1/2} \in [0, r_p]$, $j \in [0; N]$, where the r_p is the plasma radius in the incoming flow, and the staggered grid forms $N + 1/2$ grid cells. It is convenient to consider a uniform flux grid so the flux through each cell is the same $\Delta\Phi$, where:

$$\Delta\Phi = \frac{1}{N + 1/2} \int_0^{r_p} B_{z0}(r) \pi \mathrm{d}(r^2). \tag{3.21}$$

The following relations can be written for the cell centers and boundaries:

$$\int_{r_{j-1}}^{r_j} B_{z0}(r) \pi \mathrm{d}(r^2) = \Delta\Phi, \tag{3.22}$$

$$\int_{r_{j-1}}^{r_{j-1/2}} B_{z0}(r) \pi \mathrm{d}(r^2) = \frac{\Delta\Phi}{2}, \tag{3.23}$$

where $j \in [1, N]$, $r_0 = 0$ and $r_{N+1/2} = r_p$.

We determine r and B_r/B_z in integer positions j (cell boundaries) and the other quantities are computed in half-integer grid points $j + 1/2$ (cell centers).

The finite difference equations corresponding to Eqs. (3.7) - (3.9) have the following form:

$$\left[\frac{\partial r}{\partial z} \right]_j = \left[\frac{B_r}{B_z} \right]_j, \qquad j = 1, \ldots, N, \tag{3.24}$$

$$\left[\frac{\partial}{\partial z}\left(\frac{B_r}{B_z}\right)\right]_j = -\pi r_j \left(\left[\frac{B_z}{\Pi_{||}}\right]_{j+1/2} + \left[\frac{B_z}{\Pi_{||}}\right]_{j-1/2}\right) \frac{[P_{tot}]_{j+1/2} - [P_{tot}]_{j-1/2}}{\Delta\Phi}, \tag{3.25}$$

$$j = 2, \ldots, N,$$

$$\left(\frac{B_r}{B_z}\right)_1 = 0, \tag{3.26}$$

where $P_{tot} = \Pi_\perp + B_z^2/(8\pi)$ is the total pressure. The Eq. (3.26) is the no-penetration boundary condition at the system axis which leads to vanishing of all vector fields components normal to the non-penetrable surface ($r_0 = 0$ in this case).

The axial magnetic field is determined as:

$$[B_z]_{j+1/2} = \frac{1}{\pi} \frac{\Delta\Phi}{(r^2)_{j+1} - (r^2)_j}, \qquad j = 0, 1, \ldots, N-1. \tag{3.27}$$

The boundary value of the axial magnetic field $(B_z)_{N+1/2}$ can be obtained from the plasma-vacuum boundary condition:

$$n_{i0} x^2 \frac{I_\perp(x)}{I_n(1)} + x^2 \frac{B_{z0}^2}{8\pi} = \frac{\left[B_z^{(v)}(z)\right]^2}{8\pi}, \tag{3.28}$$

where $(B_z)_{N+1/2} = x(B_{z0})_{N+1/2}$. The nonlinear equation with respect to x is solved by Newton-Raphson root finder method at the fixed location z along the axis. The function $B_z^{(v)}(z)$ is assumed to be computed independently from the vacuum magnetic field solution.

The above system can be normalized for the effective numerical implementation. The values of r_0, r and $\tilde{z}$ are normalized over the initial plasma radius r_p. The ion density and z-component of the magnetic field B_z can be normalized over the peak values of the initial profiles n_{i0max} and B_{z0max}

correspondingly. The ion energies can be normalized over the characteristic magnetic field energy $B_{z0max}^2/(8\pi n_{i0max})$.

The system of Eqs. (3.24), (3.25) is solved using the explicit Runge-Kutta solver of order (2,3) with Bogacki-Shampine pair [5]. The above described Lagrangian one-dimensional scheme does not require ALE (Arbitrary Lagrangian-Eulerian) style remapping and rezoning stages due to the fact that the flow under consideration is a supersonic and super-Alfvénic therefore no shocks or discontinuities appear in the flow.

3.2 Numerical implementation of the vacuum magnetic field solver

We discretize the vector potential equation using the second-order central finite differences:

$$\frac{A_{i+1,j} - 2A_{i,j} + A_{i-1,j}}{\Delta_r^2} + \frac{A_{i,j+1} - 2A_{i,j} + A_{i,j-1}}{\Delta_z^2} + \frac{1}{r_i}\frac{A_{i+1,j} - A_{i-1,j}}{2\Delta_r} - \frac{A_{i,j}}{r_i^2} = -4\pi J_{i,j}. \tag{3.29}$$

The plasma-vacuum interface $r_{pv}(z)$ is stair-step interpolated and all grid nodes at the interpolated boundary and below are set to zero according to the plasma-vacuum boundary condition, i.e. $A_{i,j} = 0$, $i, j \in$ plasma. The boundary condition at $z = z_0$ is simple Dirichlet boundary condition with fixed values of the vector potential at the boundary nodes $A_{i,0} = A_i^{(src)}$.

There are several possible treatments of the open boundaries [17]. The simplest one is a truncation boundary condition, where we set $A = 0$ at the boundaries. It can suffer some accuracy problems for the case when the boundaries are not far enough from the source. The more precise way to handle the open boundaries is the asymptotic boundary conditions. In cylindrical coordinates and axisymmetric case the open boundary conditions for the magnetic vector potential can be written as (Appendix C):

$$r\frac{\partial A}{\partial r} + z\frac{\partial A}{\partial z} + 2A = 0, \tag{3.30}$$

and at $z = z_{max}$ and $r = r_{max}$ they can be discretized in the following way:

$$r_i\frac{A_{i+1,j} - A_{i-1,j}}{2\Delta_r} + z_j\frac{A_{i,j+1} - A_{i,j-1}}{2\Delta_z} + 2A_{i,j} = 0. \tag{3.31}$$

The finite-difference grid consists of inner nodes ($i = 1, \ldots, M$, $j = 1, \ldots, N$) and halo or ghost nodes($i = 0$, $j = 0$, $i = M + 1$, $j = N + 1$). In the case of Dirichlet boundary conditions the values in the halo nodes are not used and can be set to zero. The above equations (3.29), (3.31) are written for the inner nodes. The corner inner nodes require the special treatment in case of Neumann or mixed boundary conditions since it depends on two ghost nodes. In this case the boundary condition equation in this node must be written twice, where the central difference will be replaced with appropriate forward or backward difference to remove one unknown. We have only one corner node with non-Dirichlet boundary condition in this case which corresponds to $z = z_{max}$, $r = r_{max}$ point. One can write the following finite-difference equations:

$$r_M\frac{3A_{M,N} - 4A_{M-1,N} + A_{M-2,N}}{2\Delta_r} + z_N\frac{A_{M,N+1} - A_{M,N-1}}{2\Delta_z} + 2A_{M,N} = 0, \tag{3.32}$$

$$r_M\frac{A_{M+1,N} - A_{M-1,N}}{2\Delta_r} + z_N\frac{3A_{M,N} - 4A_{M,N-1} + A_{M,N-2}}{2\Delta_z} + 2A_{M,N} = 0. \tag{3.33}$$

Forming the vector from the grid points values one can write the linear equation in the matrix form. The resulting matrix is sparse block-diagonal matrix and it can be solved by iterative method for the system of linear equations.

One of the effective procedures for this is Bi-Conjugate Gradient method [15], which produces fast converging iterations and it can be effectively implemented in the parallel frameworks. Once the vector potential values on the grid are found, one can calculate the axial component of the magnetic field at the plasma-vacuum interface as:

$$(B_z)_{1,j} = \frac{4A_{2,j} - A_{3,j}}{2\Delta_r}, \tag{3.34}$$

where we have used the backward finite difference derivative with plasma vacuum boundary condition $A_{1,j} = 0$.

Chapter 4

Code benchmarking and simulation results

4.1 Benchmarking

To benchmark the code, consider a highly super-Alvénic flow of a cold plasma that comes out of a conical magnetic nozzle (all energy is in the longitudinal ion motion along the magnetic field lines, i.e. $\varepsilon_{\perp} = 0$). The analytical solution for the case without a vacuum gap between the plasma and the nozzle wall was first presented in Ref. [2]. The alternative path to derive the conical nozzle analytic solution can be developed by using self-similar solution technique. Using the Eqs. (2.33), (2.54), the governing system of equations in this case can be written in the following form:

$$\left(\frac{\partial}{\partial z} + \frac{B_r}{B_z}\frac{\partial}{\partial r}\right) B_z = -B_z \frac{1}{r}\frac{\partial}{\partial r}\left(r\frac{B_r}{B_z}\right), \tag{4.1}$$

$$\left(\frac{\partial}{\partial z} + \frac{B_r}{B_z}\frac{\partial}{\partial r}\right) \frac{B_r}{B_z} = -\frac{B_z}{8\pi n_i \varepsilon_{||}}\frac{\partial B_z}{\partial r}, \tag{4.2}$$

$$\left(\frac{\partial}{\partial z} + \frac{B_r}{B_z}\frac{\partial}{\partial r}\right) \varepsilon_{||} = 0. \tag{4.3}$$

$$\left(\frac{\partial}{\partial z} + \frac{B_r}{B_z}\frac{\partial}{\partial r}\right) \left(\frac{8\pi n_i \varepsilon_{||}}{B_z}\right) = 0. \tag{4.4}$$

In an infinitely long conical nozzle with a perfectly conducting wall located at $r(z) = z\tan\theta_0$, the boundary condition at the nozzle wall is the continuity of the normal component of the magnetic field. The magnetic field outside the wall is zero, hence $B_r\cos\theta_0 - B_z\sin\theta_0 = 0$. The radial component of the magnetic field vanishes at the nozzle axis ($r = 0$) due to the system symmetry. Therefore we can construct the following solution for the magnetic field for $z > z_0$:

$$\frac{B_r}{B_z} = \frac{r}{z}, \qquad B_z = B_{z0}\frac{z_0^2}{z^2}, \tag{4.5}$$

where B_{z0} is the value of the z-component of the magnetic field at the nozzle entrance position z_0. The solution indicates that the magnetic field lines are straight and starting at the coordinate system origin. The plasma motion is decoupled from the magnetic field configuration in this case and the solution for the Eqs. (4.3),(4.4) is not unique. The simplest choice is the radially uniform ion density and kinetic energy. In this case we obtain for $z > z_0$:

$$\varepsilon_{||} = \varepsilon_{||0}, \qquad n_i = \frac{z_0^2}{z^2} n_{i0}. \tag{4.6}$$

In the case of a finite-length conical nozzle (Fig. 4.1), the solution inside the nozzle ($z \in [z_0, z_*]$, where z_* is the z-coordinate of the nozzle throat) is still given by Eqs. (4.5), (4.6), provided that the outgoing flow is highly super-Alfvénic (no perturbations propagating backward) and that there is no vacuum gap between the plasma and the nozzle wall. The plume consists of an unperturbed main flow [Eqs. (4.5), (4.6)] and a rarefaction wave at the flow edge.

The rarefaction wave is localized in a thin layer between the vacuum and the unperturbed main plasma flow. To find the solution in the rarefaction wave, we present B_r/B_z in the form:

$$\frac{B_r}{B_z} = \frac{r}{z} + \delta\theta, \tag{4.7}$$

where r/z is the unperturbed main flow solution (essentially the slope of the magnetic field line without the rarefaction wave) and $\delta\theta$ is a small correction

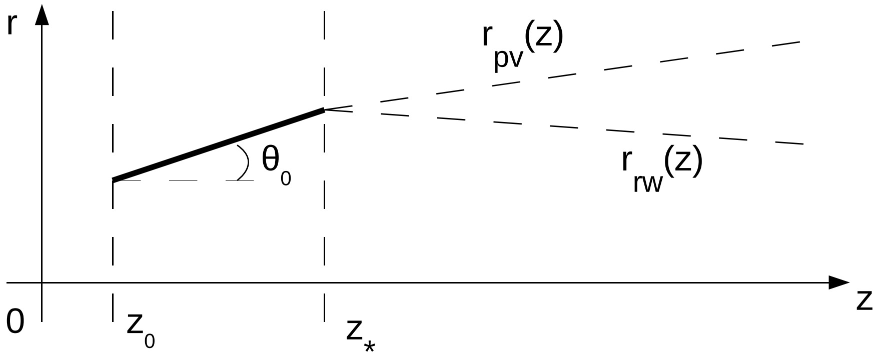

Figure 4.1: The geometry of a conical nozzle. The nozzle wall is shown as a thick solid line. The rarefaction wave (hatched region) is bounded by the inner front line $r = r_{rw}(z)$ (the outer boundary of an unperturbed plasma flow) and outer front line $r = r_{pv}(z)$ (plasma-vacuum boundary).

associated with the wave. We use the definition (4.7) to rewrite Eqs. (4.1) - (4.4):

$$\left[\frac{\partial}{\partial z} + \left(\frac{r}{z} + \delta\theta\right)\frac{\partial}{\partial r}\right] B_z = -\frac{2B_z}{z} - B_z\frac{\partial}{\partial r}\left(\delta\theta\right), \tag{4.8}$$

$$\left[\frac{\partial}{\partial z} + \left(\frac{r}{z} + \delta\theta\right)\frac{\partial}{\partial r}\right] \delta\theta = -\frac{\delta\theta}{z} - \frac{B_z}{8\pi n_i \varepsilon_{||}}\frac{\partial B_z}{\partial r}, \tag{4.9}$$

$$\left[\frac{\partial}{\partial z} + \left(\frac{r}{z} + \delta\theta\right)\frac{\partial}{\partial r}\right] \left(\frac{8\pi n_i \varepsilon_{||}}{B_z}\right) = 0, \tag{4.10}$$

$$\left[\frac{\partial}{\partial z} + \left(\frac{r}{z} + \delta\theta\right)\frac{\partial}{\partial r}\right] \varepsilon_{||} = 0, \tag{4.11}$$

where we neglected the term $B_z\delta\theta/r$ in Eq. (4.8). This term is much smaller than $B_z\partial(\delta\theta)/\partial r$, because $\delta\theta$ varies in a thin layer in the highly super-Alfvénic flow.

The non-derivative terms in the Eqs. (4.8) and (4.9) can be eliminated by the replacing of the unknown functions B_z and $\delta\theta$ by new functions $\tilde{B}_z =$

$B_z z^2/z_*^2$ and $\tilde{\delta\theta} = \delta\theta z/z_*$ correspondingly. We also set $\chi^2 = (8\pi n_i \varepsilon_{||})/B_z$. As a result we get:

$$\left[\frac{\partial}{\partial z} + \left(\frac{r}{z} + \frac{z_* \tilde{\delta\theta}}{z}\right)\frac{\partial}{\partial r}\right]\tilde{B}_z = -\tilde{B}_z \frac{z_*}{z}\frac{\partial}{\partial r}\left(\tilde{\delta\theta}\right), \tag{4.12}$$

$$\left[\frac{\partial}{\partial z} + \left(\frac{r}{z} + \frac{z_* \tilde{\delta\theta}}{z}\right)\frac{\partial}{\partial r}\right]\tilde{\delta\theta} = -\frac{1}{\chi^2}\frac{z_*}{z}\frac{\partial \tilde{B}_z}{\partial r}, \tag{4.13}$$

$$\left[\frac{\partial}{\partial z} + \left(\frac{r}{z} + \frac{z_* \tilde{\delta\theta}}{z}\right)\frac{\partial}{\partial r}\right]\chi = 0, \tag{4.14}$$

$$\left[\frac{\partial}{\partial z} + \left(\frac{r}{z} + \frac{z_* \tilde{\delta\theta}}{z}\right)\frac{\partial}{\partial r}\right]\varepsilon_{||} = 0. \tag{4.15}$$

It is convenient to make a coordinate transformation in order to describe the rarefaction wave which originates at the nozzle throat.

$$r' = \frac{z_*}{z}\left(r - z\theta_0\right) \qquad z' = \frac{z_*}{z}\left(z - z_*\right), \tag{4.16}$$

where $r' = 0$, $z' = 0$ correspond to the nozzle throat wall position.

Hence the derivatives in new coordinates can be written as:

$$\frac{z_*}{z}\frac{\partial}{\partial r'} = \frac{\partial}{\partial r}, \tag{4.17}$$

$$\frac{z_*^2}{z^2}\frac{\partial}{\partial z'} = \frac{\partial}{\partial z} + \frac{r}{z}\frac{\partial}{\partial r}. \tag{4.18}$$

As a result, the governing system of equations becomes

$$\left[\frac{\partial}{\partial z'} + \tilde{\delta\theta}\frac{\partial}{\partial r'}\right]\tilde{B}_z = -\tilde{B}_z \frac{\partial}{\partial r'}\tilde{\delta\theta}, \tag{4.19}$$

$$\left[\frac{\partial}{\partial z'} + \tilde{\delta\theta}\frac{\partial}{\partial r'}\right]\tilde{\delta\theta} = -\frac{1}{\chi^2}\frac{\partial}{\partial r'}\tilde{B}_z, \tag{4.20}$$

$$\left[\frac{\partial}{\partial z'} + \tilde{\delta\theta}\frac{\partial}{\partial r'}\right]\chi = 0, \tag{4.21}$$

$$\left[\frac{\partial}{\partial z'} + \tilde{\delta\theta}\frac{\partial}{\partial r'}\right]\varepsilon_{||} = 0. \tag{4.22}$$

The main flow solution in new variable can be written as:

$$\tilde{B}_z = B_{z*}, \qquad \tilde{\delta\theta} = 0, \qquad \chi = \mathrm{M}_{\mathrm{A}*}B_{z*}^{1/2}, \qquad \varepsilon_{||} = \varepsilon_{||*}, \tag{4.23}$$

where $B_{z*} = B_{z0}z_0^2/z_*^2$, $\mathrm{M}_{\mathrm{A}*}$ and $\varepsilon_{||*} = \varepsilon_{||0}$ are z-component of the magnetic field, the Alfvénic Mach number and the ion kinetic energy at the nozzle throat correspondingly. The Alfvénic Mach number, which is the ratio of the ion velocity to the Alfvén velocity is determined as:

$$\mathrm{M}_{\mathrm{A}*} = \left(\frac{8\pi n_{i*}\varepsilon_{||*}}{B_{z*}^2}\right)^{1/2}, \tag{4.24}$$

where $n_{i*} = n_{i0}z_0^2/z_*^2$.

Introducing the self-similar variable $\xi = r'/z' = (r - z\theta_0)/(z - z_*)$ one can rewrite the Eqs. (4.19)-(4.22) in the following form:

$$\left[\tilde{\delta\theta} - \xi\right]\frac{\partial\tilde{B}_z}{\partial\xi} = -\tilde{B}_z\frac{\partial}{\partial\xi}\left(\tilde{\delta\theta}\right), \tag{4.25}$$

$$\left[\tilde{\delta\theta} - \xi\right]\frac{\partial\tilde{\delta\theta}}{\partial\xi} = -\frac{1}{\chi^2}\frac{\partial\tilde{B}_z}{\partial\xi}, \tag{4.26}$$

$$\frac{\partial\chi}{\partial\xi} = 0, \tag{4.27}$$

$$\frac{\partial\varepsilon_{||}}{\partial\xi} = 0. \tag{4.28}$$

Requiring a non-trivial solution of the Eqs. (4.25) - (4.28) one can write the following condition:

$$\left[\tilde{\delta\theta} - \xi\right]^2 = \frac{1}{\chi^2}\tilde{B}_z. \tag{4.29}$$

Hence up to the sign value $s = \pm 1$ it can be resolved as:

$$\tilde{\delta\theta} - \xi = s\frac{1}{\chi}\tilde{B}_z^{1/2}. \tag{4.30}$$

Substituting the Eq. (4.30) into Eq. (4.25) and using Eq. (4.27) we get:

$$\frac{\partial}{\partial \xi}\left(2s\frac{1}{\chi}\tilde{B}_z^{1/2}+\tilde{\delta\theta}\right)=0. \tag{4.31}$$

The Eqs. (4.27), (4.28) and (4.31) can be integrated using the boundary condition at the interface between the unperturbed main flow and the rarefaction wave $\xi=\xi_{rw}$. Therefore,

$$\varepsilon_{||}=\varepsilon_{||*}, \qquad \chi=\mathrm{M}_{\mathrm{A}*}B_{z*}^{1/2}, \qquad 2s\frac{1}{\mathrm{M}_{\mathrm{A}*}}\sqrt{\frac{\tilde{B}_z}{B_{z*}}}+\tilde{\delta\theta}=2s\frac{1}{\mathrm{M}_{\mathrm{A}*}}. \tag{4.32}$$

From Eq. (4.30) we get

$$\tilde{\delta\theta}-\xi=s\frac{1}{\mathrm{M}_{\mathrm{A}*}}\sqrt{\frac{\tilde{B}_z}{B_{z*}}}, \tag{4.33}$$

and at the interface between plasma and the rarefaction wave

$$\xi_{rw}=-s(1/\mathrm{M}_{\mathrm{A}*}). \tag{4.34}$$

The relation (4.34) suggest the choice of the sign constant s. The Alfvén Mach number is positive and $\xi_{rw}=(r_{rw}(z)-z\theta_0)/(z-z_*)<0$ because the rarefaction wave is the perturbation of the main flow with boundary $r=z\theta_0$ running into and out of the main flow. Hence $s=1$.

Thus we obtain:

$$\sqrt{\frac{\tilde{B}_z}{B_{z*}}}=\frac{1}{3\xi_{rw}}\left(\xi+2\xi_{rw}\right), \tag{4.35}$$

$$\tilde{\delta\theta}(r,z)=\frac{2}{3}\left(\xi-\xi_{rw}\right). \tag{4.36}$$

The plasma-vacuum boundary position can be determined from Eq. (4.35) using the fact that the magnetic field vanishes there. Hence $\xi_{pv}=-2\xi_{rw}$.

Thus the solution in all regions of the plasma flow is constructed. By returning to original variables one can write the rarefaction wave solution as:

$$B_z(r,z) = B_{z*}\frac{z_*^2}{z^2}\frac{1}{9}\left(-M_{\mathrm{A}*}\frac{r-\theta_0 z}{z-z*}+2\right)^2, \tag{4.37}$$

$$\frac{B_r}{B_z}(r,z) = \frac{r}{z}+\frac{2}{3}\frac{z_*}{z}\left(\frac{r-\theta_0 z}{z-z*}+\frac{1}{M_{\mathrm{A}*}}\right), \tag{4.38}$$

$$n_i(r,z) = n_{i*}\frac{B_z}{B_{z*}}, \tag{4.39}$$

$$\varepsilon_{||}(r,z) = \varepsilon_{||*}, \tag{4.40}$$

where $r \in [r_{rw}, r_{pv}]$ and

$$r_{pv} = z\theta_0 + \frac{2}{M_{\mathrm{A}*}}(z-z_*) \tag{4.41}$$

is the location of the plasma-vacuum interface and

$$r_{rw} = z\theta_0 - \frac{1}{M_{\mathrm{A}*}}(z-z_*) \tag{4.42}$$

is the location of the inner wave front [1]. The required values at the nozzle throat location are $B_{z*} = B_{z0}z_0^2/z_*^2$, $n_{i*} = (z_0^2/z_*^2)n_{i0}$ and $\varepsilon_{||*} = \varepsilon_{||0}$. A plot of the solution given by Eqs. (4.5), (4.5), (4.37), (4.38) is shown in Fig. 4.2.

In order to simulate the conical nozzle shown in Fig. 4.1, with a divergence angle θ_0 and minimal nozzle radius r_p, the magnetic field B_{z0}, ion density n_{i0} and incoming ion kinetic energy $\varepsilon_{||0}$ values must be set at the nozzle entrance as initial conditions. Inside the nozzle, where $z \in [z_0, z_*]$, we impose that the magnetic field boundary conditions corresponding the value of the

---

[1] The expression for r_{rw} given here by Eq. (4.42) is slightly different from that given by Eq. (77) in Ref. [2]. Equation (4.42) is a linear expansion of Eq. (77) with respect to the small parameter $1/\theta_0 M_A \ll 1$.

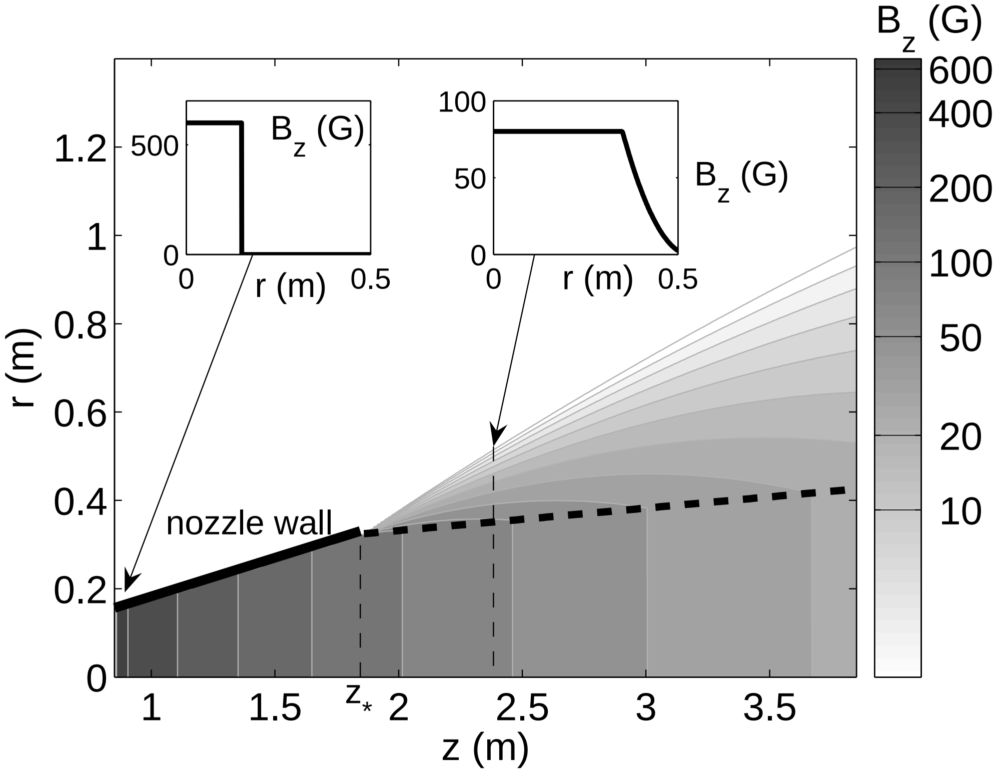

Figure 4.2: Analytical solution for a highly super-Alfvénic cold plasma flow coming out of a conical magnetic nozzle with a divergence angle $\theta_0 = 10°$. The contours show the levels of constant B_z, with the scale indicated on the sidebar. The thick dashed line marks the inner front of the rarefaction wave $r_{rw}(z)$. The incoming flow parameters at the nozzle entrance ($z_0 = 0.87$ m) are $n_i = 5.0 \cdot 10^{20}$ m^{-3}, $\varepsilon_{||} = 250$ eV, $r_p = 0.15$ m and $B_{z0} = 600$ G. The Alfvénic Mach numbers at the nozzle entrance ($z = z_0$) and the nozzle exit ($z_* = 1.87$ m) are $M_{\mathrm{A}0} = 3.74$ and $M_{\mathrm{A}*} = 17.3$. The insets give radial profiles of B_z in the incoming flow ($z = z_0$) and in the plume ($z = 2.37$ m).

magnetic field on the infinite nozzle wall $B_p = B_{z0} r_p^2 / (z^2 \theta_0^2)$. To simulate the rarefaction wave, we impose a sharply decreasing magnetic field at the plasma boundary downstream from the nozzle exit ($z > z_*$). The pattern of the rarefaction wave is insensitive to the details of the decrease, as long as the field decreases with z much faster than $B_{z0} r_p^2 / (z^2 \theta_0^2)$. For example, the following boundary condition can be used:

$$B_p = \frac{B_{z0}}{z^2 \theta_0^2} \left(r_p^2 + (R_H^2 - r_p^2) \theta_H (z - z_*) \right) \tag{4.43}$$

where $R_H << r_p$ and $\theta_H(z - z_*)$ is Heaviside step function.

Note that the axial coordinate z is defined such that the nozzle's wall is located at $r = \theta_0 z$ for $z_0 \leq z \leq z_*$.

Fig. 4.3 shows a well pronounced rarefaction wave at the plasma boundary. As expected, the central part of the flow remains unperturbed. The good agreement between Fig. 4.2 and Fig. 4.3 ensures that the code is reasonably accurate.

4.2 Numerical examples of plasma detachment

Simulations presented in this subsection involve transition from sub- to super-Alfvénic flow. The first example refers to cold ions with an initial velocity directed along the guiding magnetic field. We consider a cylindrical nozzle with a vacuum gap between the plasma and the nozzle wall. The magnetic coils represent a long (semi-infinite) solenoid with an inner radius of $R = 0.25$ m and with a uniform current distribution in the coils. The incoming plasma radius is $r_p = 0.15$ m. The ion energy in the incoming plasma flow is $\varepsilon_{||} = 10$ eV, the incoming density is $n_{i0} = 5.0 \cdot 10^{20}$ m^{-3}. These parameters correspond to the power level of 395 kW for argon plasma. The magnetic field

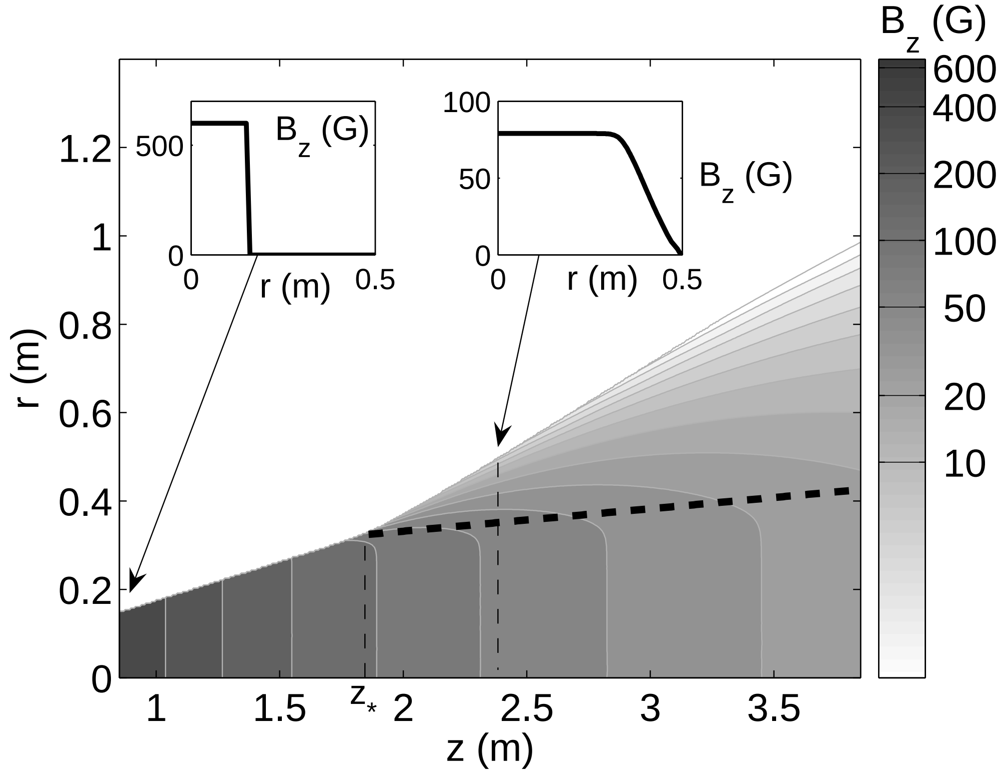

Figure 4.3: Simulation results for a highly super-Alfvénic flow coming out of a conical magnetic nozzle. The nozzle divergence angle and the incoming flow parameters are the same as in Fig. 4.2. The thick dashed line marks the inner front of the rarefaction wave $r_c(z)$ in the analytical solution.

deep inside the nozzle is 600 G. Fig. 4.4 shows the behavior of the Alfvénic Mach number M_A in the plasma jet. The thick solid line separates the sub- and super-Alfvénic regions in the plasma flow. The sub- to super-Alfvénic transition occurs somewhat outside the solenoid, close to its end. The shape of the shaded area in the plot shows that the plasma plume does not follow the vacuum magnetic field lines from the solenoid, which is a clear evidence of detachment. This conclusion also follows from calculations of detachment efficiency (see Sec. 4.3).

The second example demonstrates detachment together with conversion of ion gyro-energy into directed energy of the plasma jet. The nozzle is again a semi-infinite solenoid with the inner radius $R = 0.25$ m. The incoming plasma radius is $r_p = 0.1$ m and the incoming ion gyro-energy is $\varepsilon_\perp = 100$ eV, which is the same for all ions. The longitudinal energy is $\varepsilon_{||} = 10$ eV without any spread in parallel velocities. The ion density is $n_{i0} = 5.0 \cdot 10^{20}$ m^{-3}. The corresponding power is 193 kW for argon plasma. A contour plot of the transverse-to-longitudinal energy ratio presented in Fig. 4.5 shows that the conversion of the ion gyro-energy into the energy of directed flow facilitates detachment. Note that the plasma plume has a very small divergence angle far away from the nozzle, where the ions are strongly super-Alfvénic and have almost no gyro-energy left.

4.3 Nozzle efficiency

A measure of the thruster performance related to the degree of plasma detachment from the magnetic nozzle is called "nozzle efficiency". This term requires some clarification when it is used as a quantitative characteristic. One can define efficiency in terms of power or in terms of thrust. The energy flux

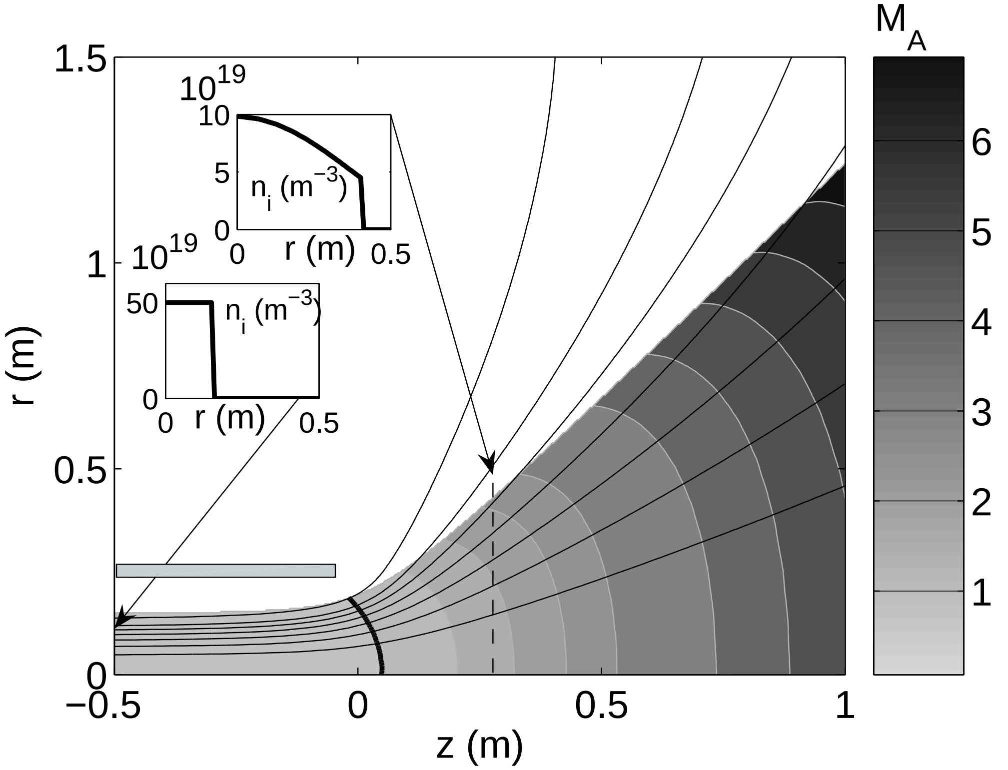

Figure 4.4: Sub- to super-Alfvénic transition in the plume of a cylindrical nozzle. The contours show the levels of constant Alfvénic Mach number M_A, with the scale indicated on the side-bar. The thick solid line separates the sub- and super-Alfvénic regions in the cold plasma flow. The light gray bar marks the location of the solenoid coils and the thin solid lines are the magnetic field lines of the solenoid in the absence of plasma. The insets give radial profiles of n_i in the incoming flow ($z = -0.5$ m) and in the plume ($z = 0.25$ m).

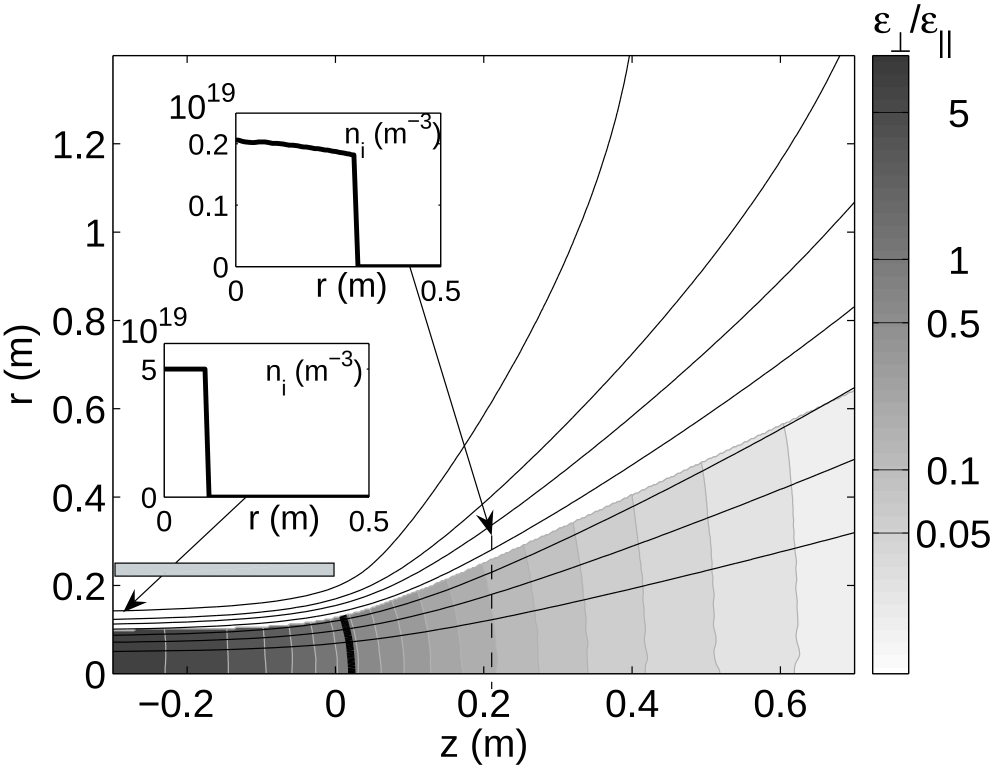

Figure 4.5: Transition from sub- to super-Alfvénic flow with a simultaneous conversion of the ion gyro-energy $\varepsilon_\perp$ into the axial energy $\varepsilon_{||}$. The contours show the levels of constant $\varepsilon_\perp/\varepsilon_{||}$ ratio. The thick solid line marks the location, where $\varepsilon_\perp/\varepsilon_{||} = 1$. The light gray bar marks the location of the solenoid coils and the thin solid lines are the magnetic field lines of the solenoid in the absence of plasma. The insets give radial profiles of n_i in the incoming flow ($z = -0.3$ m) and in the plume ($z = 0.21$ m).

density can be written as:

$$\Phi_\varepsilon = \int f \frac{m\mathrm{v}^2}{2} \mathrm{v}_z \mathrm{d}^3\mathrm{v}. \tag{4.44}$$

Hence the the power efficiency (η_P) can be represented as the ratio of the "directed" power in the plasma plume to the power in the incoming plasma flow, i.e.:

$$\eta_P = \left[\int f_\infty \mathrm{v}_z \mathrm{v}_z^2 \mathrm{d}^3\mathrm{v}\ d\left(\pi r^2\right)\right] \left[\int f_0 \mathrm{v}_z \mathrm{v}^2 \mathrm{d}^3\mathrm{v}\ \mathrm{d}\left(\pi r^2\right)\right]^{-1}, \tag{4.45}$$

where f_0 and f_∞, respectively, are the ion distribution functions at the nozzle entrance and in the plume, v_z is the axial component of the velocity, and the integration is performed over the velocity space and over the plasma cross-section.

In order to provide nozzle efficiency metric in terms of thrust it is appropriate to consider the absolute momentum flux density which is determined as:

$$\Pi = \int f m \mathrm{v} \mathrm{v}_z \mathrm{d}^3\mathrm{v}. \tag{4.46}$$

The thrust efficiency η_T can be defined as a ratio of the momentum flux in the plume to the maximum axial momentum that a given initial particle flux could potentially carry at given absolute values of the ion velocities. More specifically:

$$\eta_T = \left[\int f_\infty \mathrm{v}_z^2 \mathrm{d}^3\mathrm{v}\ d\left(\pi r^2\right)\right] \left[\int f_0 \mathrm{v}_z \mathrm{v} \mathrm{d}^3\mathrm{v}\ \mathrm{d}\left(\pi r^2\right)\right]^{-1}. \tag{4.47}$$

Both η_P and η_T can be calculated in a straightforward way based on a numerical solution of Eqs. (2.33)-(2.34). In addition to the asymptotic expressions (4.45) and (4.47), it is also useful to calculate similar quantities for intermediate axial locations, i.e. to replace f_∞ by the local distribution function f.

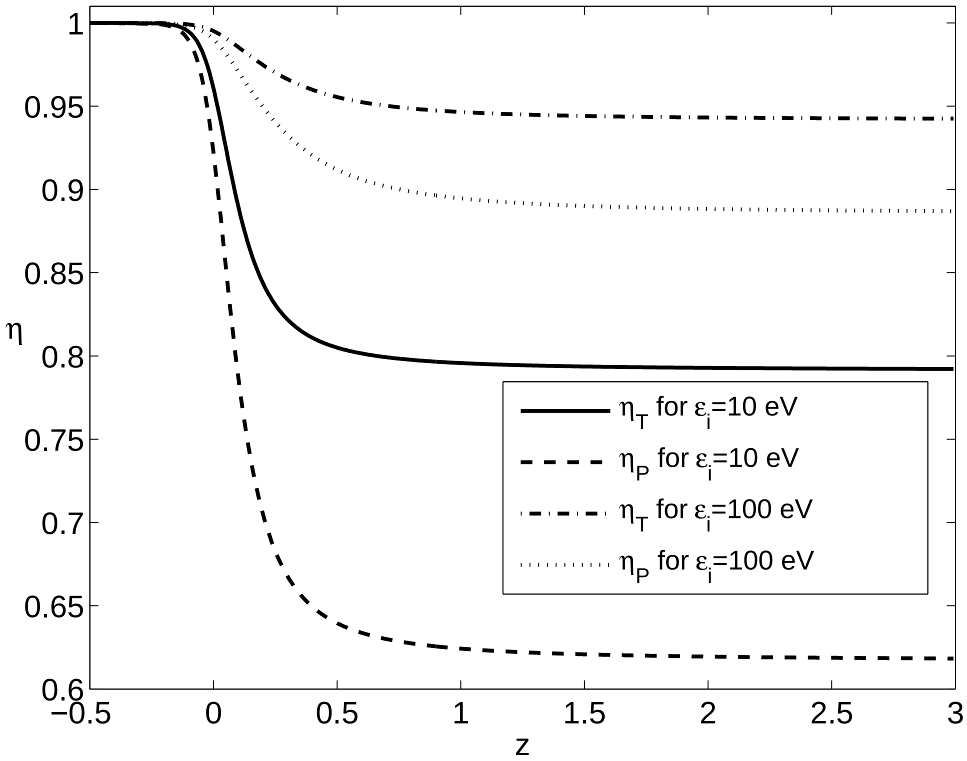

Figure 4.6: Intermediate values of the power and thrust efficiencies along the flow (dashed and solid lines) for the nozzle with the parameters of Fig. 4.4. The dotted and dash-dotted lines show $\eta_P(z)$ and $\eta_T(z)$ for ε_i=100 eV, instead of ε_i=10 eV, for the same setup.

This modification transforms η_P and η_T into functions of z. Fig. 4.6 presents the plots of $\eta_P(z)$ and $\eta_T(z)$ for the nozzle with the parameters of Fig. 4.4. For comparison, Fig. 4.6 shows the result from the simulation with a different ion energy of ε_i=100 eV. The actual efficiencies are the asymptotic values of $\eta_P(z)$ and $\eta_T(z)$, whereas the transient behavior of η_P and η_T can be viewed as an indicator of whether the flow is already detached at a given axial location.

4.4 Detachment Demonstration Experiment simulation

In order to demonstrate a plasma detachment scenario for high density, high velocity plasma flows in a diverging magnetic nozzle which is relevant to the VASIMR propulsion concept, an experiment has been performed at the NASA Marshall Propulsion Research Center, Huntsville, Alabama [10, 12]. The Detachment Demonstration Experiment (DDEX) facility was specifically designed to examine plasma behavior in a magnetic nozzle and directivity of the plasma plume. The plasma expands into a vacuum chamber with a diverging magnetic field formed by external coils. An experimental setup scheme is presented in Fig. 4.7. The large chamber (2.75 m diameter and 5 m length) with high-vacuum conditions was chosen to minimize wall effects and the charge exchange effect between ions and background neutral particles [10]. Neutral background pressure measurements taken near the plasma source show that the prepulse pressure is 2×10^{-6} Torr, reaching as high as 2×10^{-4} Torr after the pulse. Ion-neutral charge exchange effects at the highest measured pressure level such as flow deceleration and the plasma density increase were not observed in the experiment.

The plasma source in DDEX is a washer-stack gun [14] operating at 200 kW in a pulsed regime. The washer gun consists of a stack of molybdenum washers isolated by boron nitride ceramic washers. A molybdenum anode and cathode at either end of the washer stack initiate the discharge arc. The hydrogen or helium plasma plume is created by discharging a capacitor bank with the typical pulse length of 3 ms.

The magnetic field of the nozzle is created by five separately powered magnet coils: the plasma gun coil, the high field "choke" magnet coil and

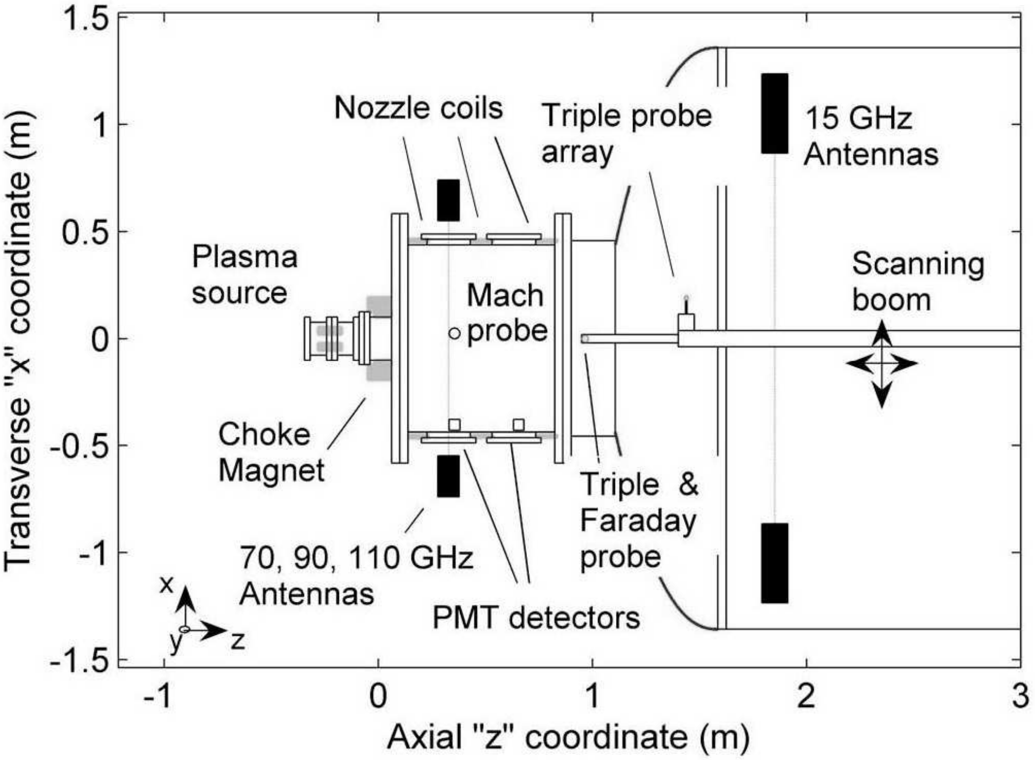

Figure 4.7: DDEX Experimental setup scheme (top view)

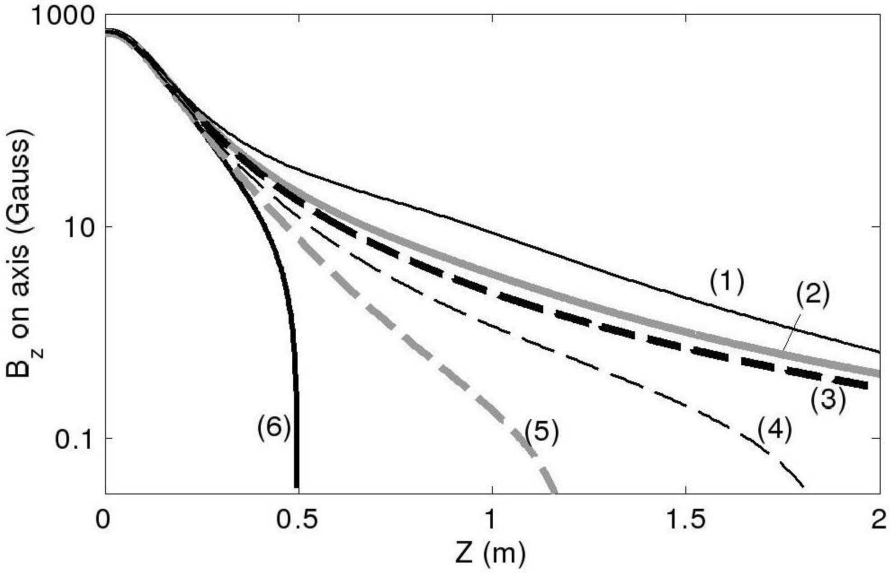

Figure 4.8: Axial magnetic field on the experiment centerline for several coil configurations

three external nozzle magnet coils wrapped around the chamber circumference. The nozzle coils can be adjusted to create different magnetic configurations. The magnetic field in the source is of the order of 0.1 Tesla, so that the flow produced by the source is sub-Alfvènic. The axial magnetic field on the experiment centerline due to external magnets is shown in 4.8. The majority of experimental measurements were performed for the magnetic configuration "2" (Fig. 4.8), which has nearly streight diverging magnetic field lines in the nozzle region.

The measurements were conducted over multiple plasma pulses to provide radial and axial profiles of plasma ion flux, velocity, electron temperature and density. The ion flux was measured by using cylindrical triple probes [11] and guarded Faraday probes [37]. A microwave interferometer was used to obtain the electron density measurements. The plasma flow velocity was estimated using the Mach probe and time of flight measurements from photomultiplier tubes (PMT) signal processing. The coordinate system used in the analysis of the experimental data is defined as follows. The origin is in the center of the choke magnet (see Fig. 4.7) and the chamber centerline corresponds to z axis.

The electron temperature is measured to be $T_e = 1.2 \pm 0.2 eV$ for the hydrogen plasma and the Mach probe measurements at $z = 0.33$ m give an ion Mach number of $M = 1.1 \pm 0.2$ which corresponds to $12 - 19$ km/s flow velocity. Time of flight analysis between two photomultipliers at $z = 0.33$ m and $z = 0.63$ m suggests an average $v_z = 15 \pm 5$ km/s between the two PMTs. Due to the nature of this diagnostic, the measurement is an average velocity between the two stationary detectors. A third measurement at the interferometer locations, $z = 0.43$ m and 1.85 m, comes from flux measurements using probes and the electron density from the probe measurement. The centerline ion flux combined with the electron density profile from the interferometers results in a flow velocity of $v_z = 17 \pm 5$ km/s. All three velocity techniques combine to suggest a constant hydrogen velocity of 16 ± 5 km/s throughout the experiment and it is corresponds roughly to 2 eV of the ion energy in the incoming flow.

The length of the pulse (3 ms) exceeds the ion travel time through the vacuum chamber by an order of magnitude. This allows the flow to reach a steady-state regime during the pulse. The interferometer measurements [3, 10] reveal that the plasma density is indeed roughly constant for about 3 ms.

All measured ion density profiles approximately followed a Gaussian

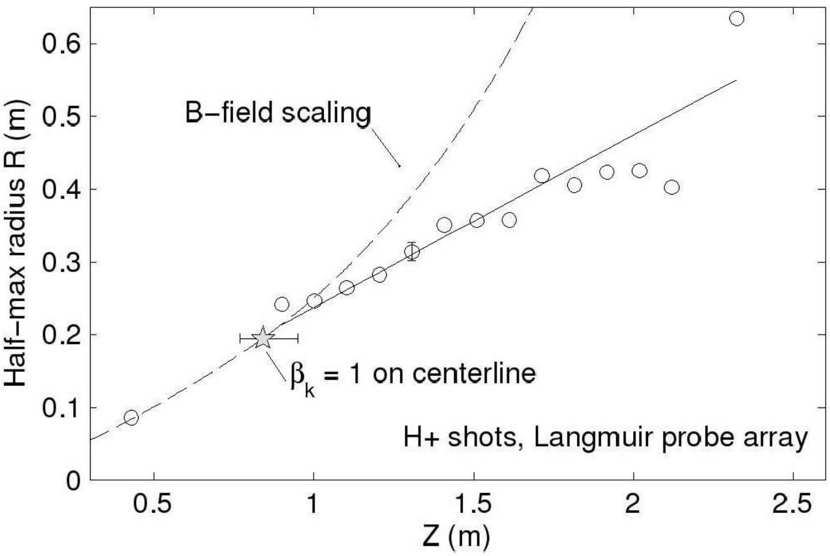

Figure 4.9: Plume radius for hydrogen shots at multiple axial positions

distribution:

$$n_i(r,z) = n_{max}(z)\exp\left(-r^2\ln 2/R^2(z)\right), \tag{4.48}$$

where $R(z)$ is the plume radius at half maximum. The plume radius $R(z)$ for the hydrogen plasma is shown in Fig. 4.9 along with the calculated plume radius in the case when the ions are tied to the vacuum magnetic field lines (no detachment case). The latter curve can be computed from the ion and magnetic flux conservation and has the following equation:

$$R(z)/R_0 = (B_{z0}/B_z(z))^{1/2}, \tag{4.49}$$

where R_0 and B_{z0} are radius and axial magnetic field at the farthest upstream probe measurement z=0.43 m. Based on the density and local velocity measurements and vacuum magnetic field value, the trasition point $z = z_1$, where $\beta = 1$ on the experiment centerline, is also plotted in Fig. 4.9. In the MHD theory for the detachment scenario it is the position where the plum separates from applied magnetic field lines and it is confirmed by the plot in Fig. 4.9. The plasma flow is tied to the magnetic field lines for $z < z_1$ and it deviates from the no-detachment curve for $z > z_1$, where $z_1 \approx 0.85$ m is the $\beta = 1$ transition point.

The plasma density profile measured at 1.85 m downstream from the plasma source is shown in Fig. 4.10 [3]. The dash-dotted line shows the density value that would correspond to a flow with measured incoming density moving strictly along the magnetic field lines produced by the external coils without any distortion by the plasma. Clearly, the measured value (circular markers with the corresponding error bars in Fig. 4.10) is significantly higher. One possible explanation of the large difference between the two density profiles is that the flow stretches the magnetic field lines. This would make the flow cross-section smaller and thus the plasma density higher compared to the case where the magnetic configuration remains unaffected by the flow. However, for this explanation to be conclusive, the background gas pressure has to be sufficiently low, so that the ion mean-free-path with respect to charge-exchange collisions is longer than the distance between the plasma source and the location where the plasma density profile is measured. In reality, this requirement is only marginally satisfied in the DDEX facility, which introduces an uncertainty in the interpretation. Nevertheless, it is still appropriate to pose the question of whether the field stretching mechanism alone can account for the observed high density in the plume.

In order to compare the experimental measurements with the MHD plasma detachment model results we carried out a simulation using the procedure described in Ch. 3. We use the experimentally measured density

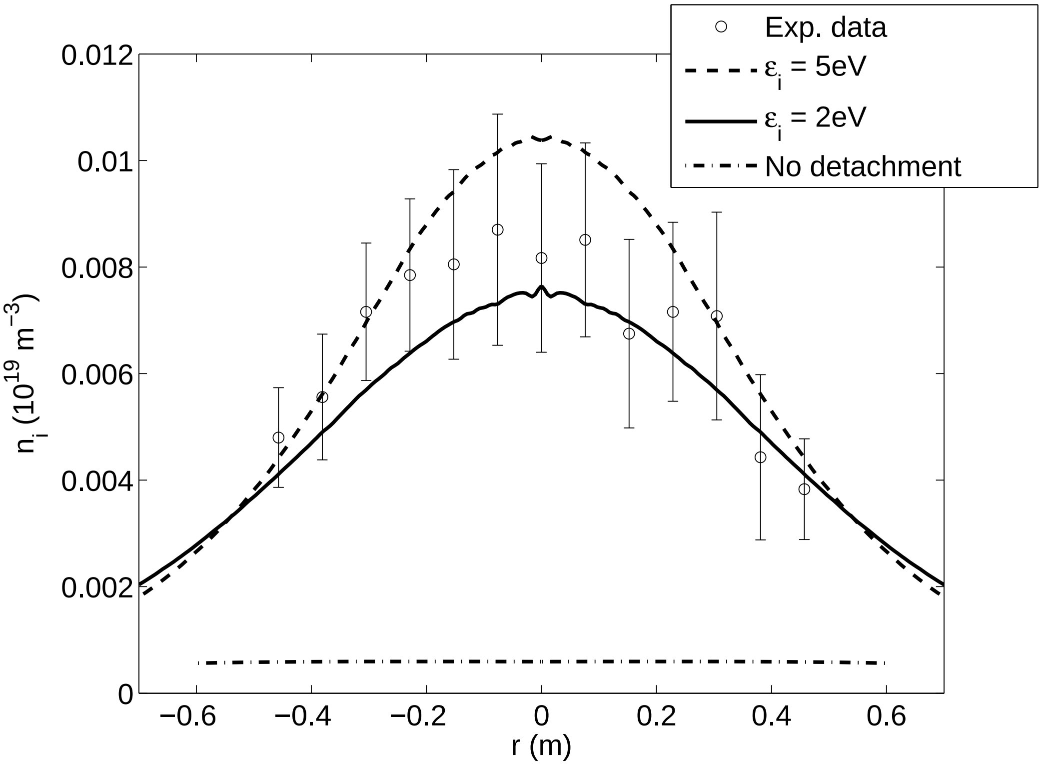

Figure 4.10: Measured and calculated radial profiles of the plasma density in DDEX. The circular markers with the corresponding error bars are the experimental data points [3]. The density value calculated under the assumption that the flow does not affect the magnetic field configuration is shown with a dash-dotted line. The solid line and dashed lines are the numerical simulation results for $\varepsilon_i = 2$ eV and $\varepsilon_i = 5$ eV, respectively.

at 0.47 m downstream from the source as an incoming flow in our calculations. The radial density profile is approximated by a Gaussian profile with $n = n_0 \exp(-r^2 \ln 2/\sigma^2)H(r_p - r)$, where $n_0 = 10^{19}$ m^{-3} is the peak density at 0.47 m, $\sigma = 0.0465$ m is the profile half-width, $r_p = 0.093$ m is the plasma radius, and H is the Heaviside step-function. The vacuum field at the plasma boundary is precalculated using the coil configuration "2" of DDEX. The ions were assumed to have no gyro-energy.

The calculated radial density profile at 1.85 m downstream from the source for the incoming flow with 2 eV ions is shown in Fig. 4.10 with a solid line. For comparison, Fig. 4.10 also shows a density profile that would correspond to 5 eV ions (dashed line). Taking into account the level of uncertainty in the experimental values of the incoming flow ion energies, the numerical simulation results showing good agreement (within a confidence range) with experimentally determined density profile.

Fig. 4.11 shows the Alfvénic Mach number for the 2 eV ions. We observe that the initially sub-Alfvénic incoming flow becomes super-Alfvénic downstream. The divergence of the plasma flow is significantly less then the divergence of the magnetic field lines calculated in the absence of plasma (thin solid lines in Fig. 4.11).

Finally, the power and thrust nozzle efficiency as functions of the experimental centerline position is shown in Fig. 4.12. The plot for 2 eV incoming flow ion energy is presented. The efficiency plot confirms the plasma detachment from the nozzle and shows the region where the flow is completely detached, i.e. where the asymptotic value is reached.

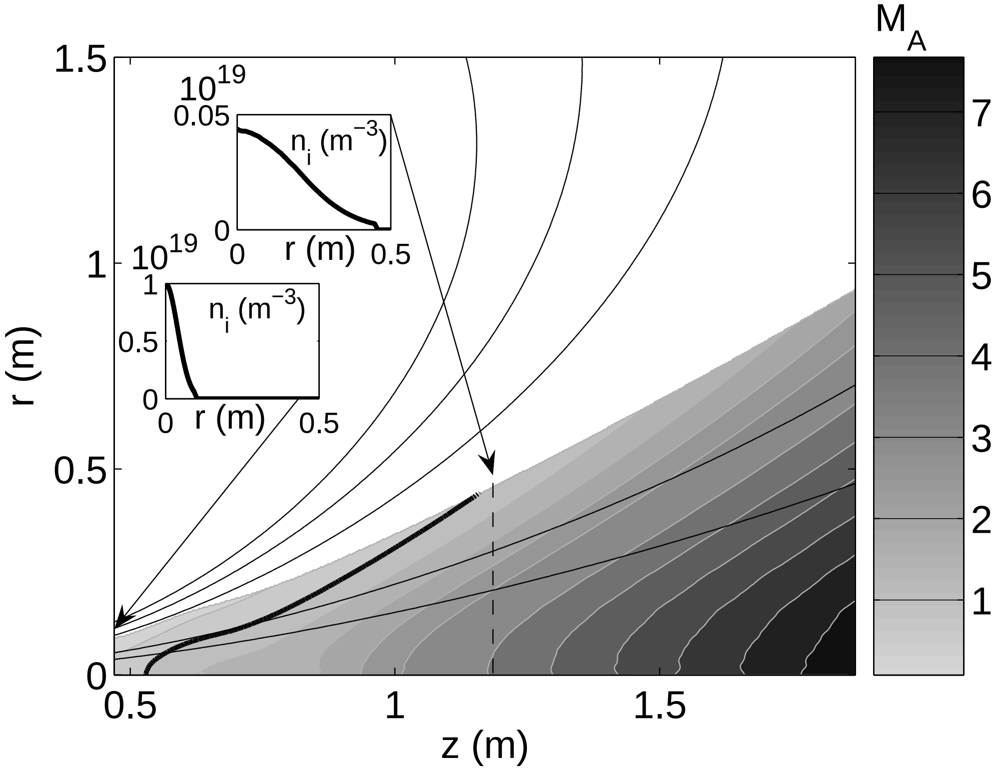

Figure 4.11: Simulation results of the plasma plume in DDEX. The contours show the levels of constant Alfvénic Mach number M_A, with the scale indicated on the side-bar. The thick solid line separates the sub- and super-Alfvénic regions. The thin solid lines are the magnetic field lines of the solenoid in the absence of plasma. The insets give radial profiles of n_i in the incoming flow ($z = 0.47$ m) and in the plume ($z = 1.17$ m).

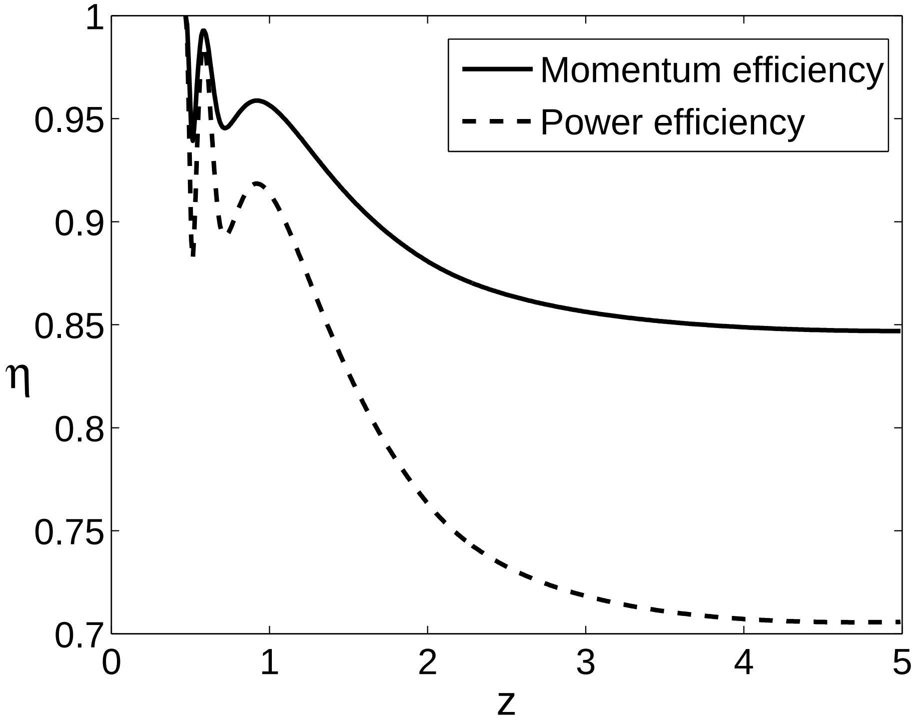

Figure 4.12: The power and thrust efficiency η plot for 2 eV incoming flow ion energy. The parameters are the same as for Fig. 4.11.

Chapter 5

Conclusions

A physics-based numerical model of plasma detachment from a magnetic nozzle for a given supersonic (but sub-Alfvénic) incoming flow is presented. Motivated by the needs of the VASIMR project, this model involves two important approximations relevant to high-power plasma thrusters. First, the choice of supersonic incoming flow helps to separate the detachment issue from the problem of creating such an input flow and allows to safely neglect any effects associated with electron pressure and the ambipolar electric field. The problem thus is reduced to dealing with a charge-neutralized ion flow in a self-consistently determined magnetic field. Second, the practical need for the nozzle to be efficient gives strong preference to slowly diverging flows with paraxial magnetic field inside the plasma, which brings significant technical simplifications into our description of a steady-state flow.

Direct solution of a steady-state problem, as opposed to an initial value problem, eliminates the need to deal with transient phenomena that are of secondary importance for continuously operating plasma thrusters. The steady-state formulation of the problem is also advantageous in terms of computational requirements, which makes the presented model suitable for exploring a range of plasma parameters and magnetic coil configurations needed to design an optimum nozzle.

The numerical code was benchmarked against the analytical solution for the rarefaction wave at the edge of the plasma plume in the conical nozzle and then used to examine situations that are not analytically tractable, including the plasma flow in a recent detachment demonstration experiment (DDEX) at the NASA Marshall Space Flight Center [3, 10, 12]. Numerical simulations for the DDEX yield density profiles in good agreement with the experimental results. It was demonstrated that a sufficiently energetic plasma can indeed detach from a magnetic nozzle. The developed numerical procedure can serve as a design tool to evaluate and optimize nozzle efficiency.

Appendices

Appendix A

Magnetic field line label

Let us consider an arc element on the magnetic field line in the axisymmetric geometry using cylindrical coordinate system $\mathrm{d}\mathbf{b} = \mathrm{d}r\mathbf{e}_r + \mathrm{d}z\mathbf{e}_z$. It must be parallel to the magnetic field, i.e. $\mathrm{d}\mathbf{b} \times \mathbf{B} = 0$. Hence $B_r\mathrm{d}z = B_z\mathrm{d}r$ or $\mathrm{d}r = B_r/B_z\mathrm{d}z$, which is an equation for the surface with axis z as an axis of symmetry. The equation for the magnetic field line can be written using some point which the field line pass through as an initial value:

$$r(z) = r(z = z_0) + \int_{z_0}^{z} \frac{B_r}{B_z}\mathrm{d}z'. \tag{A.1}$$

In some cases, it is convenient to introduce the new coordinate system related to the magnetic field lines $r_0 = r(z = z_0)$ and $\tilde{z} = z$. The coordinate transformation can be written as:

$$r = r_0 + \int_{z_0}^{\tilde{z}} \frac{B_r}{B_z}\mathrm{d}z', \qquad z = \tilde{z}. \tag{A.2}$$

The transformation Jacobian elements are:

$$\frac{\partial r}{\partial r_0} = 1 + \int_{z_0}^{\tilde{z}} \frac{\partial}{\partial r_0}\left(\frac{B_r}{B_z}\right)\mathrm{d}z', \qquad \frac{\partial r}{\partial \tilde{z}} = \frac{B_r}{B_z}, \tag{A.3}$$

$$\frac{\partial z}{\partial r_0} = 0, \qquad \frac{\partial z}{\partial \tilde{z}} = 1. \tag{A.4}$$

The partial derivatives in new coordinates are:

$$\frac{\partial}{\partial r_0} = \left(\frac{\partial r}{\partial r_0}\right)\frac{\partial}{\partial r}, \tag{A.5}$$

$$\frac{\partial}{\partial \tilde{z}} = \frac{\partial}{\partial z} + \frac{B_r}{B_z}\frac{\partial}{\partial r}. \tag{A.6}$$

The directional derivative along the magnetic field line in cylindrical coordinates has the following expression:

$$(\mathbf{b} \cdot \nabla) = \frac{B_z}{B}\left(\frac{\partial}{\partial z} + \frac{B_r}{B_z}\frac{\partial}{\partial r}\right) \tag{A.7}$$

and in the magnetic field line coordinate system it becomes:

$$(\mathbf{b} \cdot \nabla) = \frac{B_z}{B}\frac{\partial}{\partial \tilde{z}}. \tag{A.8}$$

If the directional derivative of some quantity is zero then that quantity is constant along the magnetic field lines and depends only on the r_0 coordinate which labels a magnetic field line.

In terms of the magnetic vector potential $\mathbf{B} = \nabla \times \mathbf{A}$ the magnetic field components can be written as following:

$$B_z = \frac{1}{r}\frac{\partial}{\partial r}(rA_\phi), \tag{A.9}$$

$$B_r = -\frac{\partial A_\phi}{\partial z}, \tag{A.10}$$

where A_ϕ is an azimuthal component of the magnetic potential which is the only non-zero component in the axisymmetric case. Since the magnetic field components can be expressed using the magnetic flux function Φ defined in Eq. (2.38) as:

$$B_z = \frac{1}{2\pi r}\frac{\partial \Phi}{\partial r}, \tag{A.11}$$

$$B_r = -\frac{1}{2\pi r}\frac{\partial \Phi}{\partial z}, \tag{A.12}$$

the direct comparison leads to the conclusion that:

$$\Phi = 2\pi r A_\phi = const. \tag{A.13}$$

Appendix B

Magnetic field of the current coil encircling an ideally conducting rod

The current coil has radius r_0 and it is located in the x-y plane, centered at $r = 0, z = z0$ and carries a current I which is positive as shown in Fig. B.1. It is assumed that the cross section scale of the coil is negligible, compare to its radius. The infinite ideally conducting rod with cylindrical cross section is centered at axis of symmetry (z-axis) and has radius r_c.

In cylindrical coordinates the equation for the vector potential with the current coil source has the form:

$$\frac{1}{r}\frac{\partial}{\partial r}\left(r\frac{\partial A_\phi}{\partial r}\right) + \frac{\partial^2 A_\phi}{\partial z^2} - \frac{1}{r^2}A_\phi = -\frac{4\pi}{c}I\delta(r - r_0)\delta(z - z_0). \tag{B.1}$$

Setting $A_\phi = R(r)Z(z)$ we can rewrite Eq. (B.1) for free space as:

$$\frac{1}{R}\frac{\partial^2 R}{\partial r^2} + \frac{1}{rR}\frac{\partial R}{\partial r} + \frac{1}{Z}\frac{\partial^2 Z}{\partial z^2} - \frac{1}{r^2} = 0. \tag{B.2}$$

Separating the variables, we can get the following equation for the axial part:

$$\frac{1}{Z}\frac{d^2 Z}{dz^2} = -\alpha^2, \tag{B.3}$$

with a general solution:

$$Z(z) = C_1 \sin\alpha(z - z_0) + C_2 \cos\alpha(z - z_0), \tag{B.4}$$

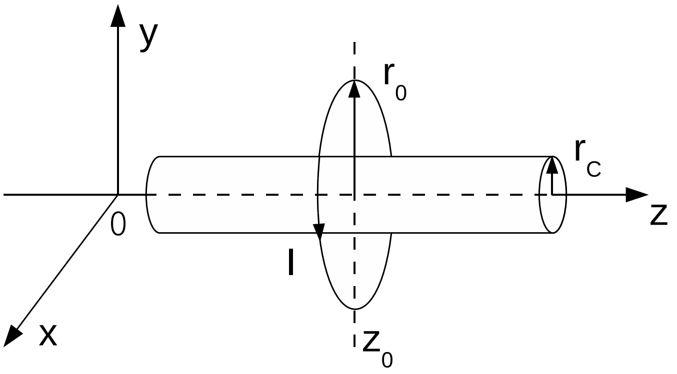

Figure B.1: The geometry of the current coil encircling an ideally conducting rod.

and the radial part we get:

$$r^2\frac{d^2R}{dr^2}+r\frac{dR}{dr}-(\alpha^2r^2+1)R=0, \tag{B.5}$$

with the solution in therms of modified Bessel functions:

$$R(r)=C_3I_1(\alpha r)+C_4K_1(\alpha r). \tag{B.6}$$

The magnetic field components can be computed as follows:

$$B_r=-R\frac{\partial Z}{\partial z},\qquad B_z=\frac{Z}{r}\frac{\partial(rR)}{\partial r}. \tag{B.7}$$

The mirror symmetry with respect to $z=z_0$ requires $B_r(r,z=z_0)=0$. At the surface of the ideal conductor $r=r_c$ the radial component of the magnetic field is zero $B_r(r=r_c,z)=0$ and it is also vanishes far from the source, i.e. $B_r(r\to\infty,z)=0$. Therefore $dZ/dz=0$ at $z=z_0$ and $R(r=r_c)=R(r\to\infty)=0$. Since $I_1(\alpha r)$ diverges at $r\to\infty$ and $\sin\alpha(z-z_0)$ is asymmetric function at $z=z_0$ we can write the solution of the problem in the following form (we drop ϕ subscript for A_ϕ in further expressions):

$$A^{(1)}(r,z) = \int_0^\infty C^{(1)}(\alpha)\left[I_1(\alpha r) - w_c K_1(\alpha r)\right]\cos\alpha(z - z_0)d\alpha, \tag{B.8}$$

$$A^{(2)}(r,z) = \int_0^\infty C^{(2)}(\alpha) K_1(\alpha r)\cos\alpha(z - z_0)d\alpha, \tag{B.9}$$

where $w_c = I_1(\alpha r_c)/K_1(\alpha r_c)$ and the region 1 is the volume $r_c < r < r_0$ and the region 2 is the volume $r > r_0$.

The radial component of the magnetic field:

$$B_r^{(1)}(r,z) = -\int_0^\infty \alpha C^{(1)}(\alpha)\left[I_1(\alpha r) - w_c K_1(\alpha r)\right]\sin\alpha(z - z_0)d\alpha, \tag{B.10}$$

$$B_r^{(2)}(r,z) = -\int_0^\infty \alpha C^{(2)}(\alpha) K_1(\alpha r)\sin\alpha(z - z_0)d\alpha, \tag{B.11}$$

and the axial magnetic field component can be obtained using the recurrence relations for the modified Bessel functions:

$$B_z^{(1)}(r,z) = \int_0^\infty \alpha C^{(1)}(\alpha)\left[I_0(\alpha r) + w_c K_0(\alpha r)\right]\cos\alpha(z - z_0)d\alpha, \tag{B.12}$$

$$B_z^{(2)}(r,z) = -\int_0^\infty \alpha C^{(2)}(\alpha) K_0(\alpha r)\cos\alpha(z - z_0)d\alpha. \tag{B.13}$$

The boundary conditions for the magnetic field at the cylindrical surface $r = r_0$, where the current coil is located, are the continuity of the normal component and the jump condition for the tangential component:

$$B_r^{(1)}\big|_{r=r_0} = B_r^{(2)}\big|_{r=r_0}, \tag{B.14}$$

$$B_z^{(1)}\big|_{r=r_0} = B_z^{(2)}\big|_{r=r_0} + \frac{4\pi I}{c}\delta(z - z_0). \tag{B.15}$$

In terms of the vector potential they can be written as

$$A^{(1)}\big|_{r=r_0} = A^{(2)}\big|_{r=r_0}, \tag{B.16}$$

$$\left.\frac{\partial A^{(1)}}{\partial r}\right|_{r=r_0} = \left.\frac{\partial A^{(2)}}{\partial r}\right|_{r=r_0} + \frac{4\pi I}{c}\delta(z-z_0). \tag{B.17}$$

Using the cosine orthogonality property:

$$\frac{1}{\pi}\int_0^\infty \cos\alpha(z-z_0)\cos\alpha'(z-z_0)d(z-z_0) = \delta(\alpha-\alpha'), \tag{B.18}$$

we can obtain the following linear system of equations for the coefficients $C^{(1)}$ and $C^{(2)}$:

$$\begin{pmatrix} I_1(\alpha r_0) - w_c K_1(\alpha r_0) & -K_1(\alpha r_0) \\ I_0(\alpha r_0) + w_c \left(\alpha K_0(\alpha r_0) - \frac{2}{r_0}K_1(\alpha r_0)\right) & K_0(\alpha r_0) \end{pmatrix} \begin{pmatrix} C^{(1)} \\ C^{(2)} \end{pmatrix} = \begin{pmatrix} 0 \\ \frac{4I}{c\alpha} \end{pmatrix}. \tag{B.19}$$

Appendix C

Open boundary conditions for the magnetic field

In order to formulate the open boundary conditions for the magnetic field let us consider the equation for the vector potential far from sources in the spherical coordinates (R,Θ,ϕ) assuming the axial symmetry:

$$\frac{1}{R^2}\frac{\partial}{\partial R}\left(R^2\frac{\partial A}{\partial R}\right)+\frac{1}{R^2\sin\Theta}\frac{\partial}{\partial\Theta}\left(\sin\Theta\frac{\partial A}{\partial\Theta}\right)-\frac{1}{R^2\sin^2\Theta}A=0. \tag{C.1}$$

Requiring $A(r\rightarrow\infty,\Theta)=0$ and $A(R,\Theta)=A(r,\Theta+2\pi)$ one can get the following solution:

$$A(R,\Theta)=\sum_{n=1}^{\infty}\frac{A_nP_n^1(\cos\Theta)}{R^{n+1}}, \tag{C.2}$$

where P_n^1 is an associated Legendre polynomial. Thus:

$$\frac{1}{R^2}\frac{\partial}{\partial R}\left(R^2A(R,\Theta)\right)=O(\frac{1}{R^3}) \tag{C.3}$$

or, neglecting high-order fast decreasing terms,

$$\frac{\partial A}{\partial R}+\frac{2}{R}A=0. \tag{C.4}$$

In cylindrical axisymmetric coordinates ($r=R\sin\Theta$, $z=R\cos\Theta$) the above expression can be written as:

$$r\frac{\partial A}{\partial r}+z\frac{\partial A}{\partial z}+2A=0. \tag{C.5}$$

It should be noted that the first term in the vector potential expansion (the one we keep) corresponds to the magnetic dipole field but the dipole moment can be calculated by integration of currents only in the case without plasma. It also suggests an alternative way of the asymptotic boundary condition derivation. Let us consider the dipole field of unknown system of currents with magnetic moment $\mathbf{m}_0$. Thus the vector potential and the magnetic field are:

$$\mathbf{A} = \frac{\mu_0}{4\pi} \frac{\mathbf{m}_0 \times \mathbf{R}}{R^3} \tag{C.6}$$

and

$$\mathbf{B} = \frac{\mu_0}{4\pi} \left(\frac{3(\mathbf{m}_0 \cdot \mathbf{R})\mathbf{R}}{R^5} - \frac{\mathbf{m}_0}{R^3} \right). \tag{C.7}$$

Taking the vector product of the radius vector and the magnetic field we get:

$$\mathbf{R} \times \mathbf{B} = \frac{\mu_0}{4\pi} \left(-\frac{\mathbf{R} \times \mathbf{m}_0}{R^3} \right) = \mathbf{A}. \tag{C.8}$$

In cylindrical coordinates and axisymmetric case we can rewrite the above equation as follows:

$$-rB_z + zB_r = A. \tag{C.9}$$

Substituting the magnetic field component expressions we get:

$$-r\frac{1}{r}\frac{\partial}{\partial r}(rA) - z\frac{\partial A}{\partial z} = A. \tag{C.10}$$

Hence:

$$r\frac{\partial A}{\partial r} + z\frac{\partial A}{\partial z} + 2A = 0. \tag{C.11}$$

Bibliography

[1] Alexey V. Arefiev and Boris N. Breizman. Theoretical components of the vasimr plasma propulsion concept. *Physics of Plasmas*, 11(5):2942–2949, 2004.

[2] Alexey V. Arefiev and Boris N. Breizman. Magnetohydrodynamic scenario of plasma detachment in a magnetic nozzle. *Physics of Plasmas*, 12(4):043504, 2005.

[3] R. D. Bengtson. (private communication), 2006.

[4] J. A. Bittencourt. *Fundamentals of Plasma Physics*. Springer, 2004.

[5] P. Bogacki and L. F. Shampine. A 3(2) pair of runge-kutta formulas. *Appl. Math. Letters*, 2:1–9, 1989.

[6] B. N. Breizman, M. R. Tushentsov, and A. V. Arefiev. Magnetic nozzle and plasma detachment model for a steady-state flow. *Phys. Plasmas*, 15:057103, 2008.

[7] Boris N. Breizman and Alexey V. Arefiev. Single-pass ion cyclotron resonance absorption. *Physics of Plasmas*, 8(3):907–915, 2001.

[8] Franklin R. Chang-Díaz. The VASIMR rocket. *Scientific American*, 283(5):90–97, November 2000.

[9] C. Charles, P. Alexander, C. Costa, O. Sutherland, R. W. Boswell, L. Pfitzner, R. Franzen, Kingwell J., A. Parfitt, P. E. Frigot, J. Gonzalez del Amo,

E. Gengembre, and G. Saccoccia. Helicon double layer thrusters. *AIAA 2006*, page 4838, 2006.

[10] D. Gregory Chavers, Chris Dobson, Jonathan Jones, Michael Lee, Adam Martin, Judith Gregory, Jim Cecil, Roger D. Bengtson, Boris Breizman, Alexey Arefiev, Franklin Chang-Diaz, Jared Squire, Tim Glover, Greg McCaskill, Jason Cassibry, and Zhongmin Li. Status of magnetic nozzle and plasma detachment experiment. *AIP Conf. Proc.*, 813(1):465–473, 2006.

[11] S. L. Chen and T. Sekiguchi. Instantaneous direct display system of plasma parameter by means of tripleprobe. *J. Appl. Phys.*, 36:2363, 1965.

[12] C. A. Deline, R. D. Bengtson, B. N. Breizman, M. R. Tushentsov, J. E. Jones, D. G. Chavers, C. C. Dobson, and B. M. Schuettpelz. Plume detachment from a magnetic nozzle. *Phys. Plasmas*, 16:033502, 2009.

[13] T. Ditmire, T. Donnelly, A. M. Rubenchik, R. W. Falcone, and M. D. Perry. Interaction of intense laser pulses with atomic clusters. *Physical Review A (Atomic, Molecular, and Optical Physics)*, 53(5):3379–3402, 1996.

[14] G Fiksel, A. F. Almagri, D. Craig, M. Lida, S. C. Prager, and J. S. Sarff. High current plasma electron emitter. *Plasma Sources Sci. Tech.*, 5:78, 1996.

[15] R. Fletcher. *Conjugate gradient methods for indefinite systems*, volume 506. Springer Berlin / Heidelberg, 1976.

[16] R. A. Gerwin, G. J. Marklin, A. G. Sgro, and A. H. Glasser. Characterization of plasma flow through magnetic nozzles. *LANL Technical Report No. AL-TR-89-092*, 1990. See National Technical Information Service Document No. DE00763033 (R. A. Gerwin, G. J. Marklin, A. G. Sgro, A. H. Glasser, LANL, Los Alamos, NM, AFOSR Technical Report AL-TR-89-092, "Characterization of Plasma Flow Through Magnetic Nozzles", 1990). Copies can be obtained from National Technical Information Service, Springfield, VA 22101.

[17] S. Gratkowski, L. Pichon, and H. Gajan. Asymtotic boundary conditions for open boundaries of axisymmetric magnetostatic finite-element models. *IEEE Trans. on Magnetics*, 38:469, 2002.

[18] R. D. Hazeltine. Recursive derivation of drift-kinetic equation. *Plasma Physics*, 15:77, 1973.

[19] E. B. Hooper. Plasma detachment from a magnetic nozzle. *Journal Of Propulsion And Power*, 9(5):757–763, September 1993.

[20] R. W. Humble, G. N. Henry, and W. J. Larson. *Space Propulsion Analysis and Design*. McGraw-Hill, 1995.

[21] T. Kammash. A fusion propulsion system for rapid interplanetary travel. *Acta Astronautica*, 47:97–102, 2000.

[22] K. Y. Kim, I. Alexeev, E. Parra, and H. M. Milchberg. Time-resolved explosion of intense-laser-heated clusters. *Physical Review Letters*, 90(2):023401, 2003.

[23] K. J. Mendham, N. Hay, M. B. Mason, J. W. G. Tisch, and J. P. Marangos. Cluster-size distribution effects in laser-cluster interaction experiments. *Physical Review A (Atomic, Molecular, and Optical Physics)*, 64(5):055201, 2001.

[24] H. M. Milchberg, S. J. McNaught, and E. Parra. Plasma hydrodynamics of the intense laser-cluster interaction. *Physical Review E (Statistical, Nonlinear, and Soft Matter Physics)*, 64(5):056402, 2001.

[25] R. W. Moses, R. A. Gerwin, and R. A. Schoenberg. unknown. *AIP Conf. Proc.*, 246:1293, 1992.

[26] E. N. Parker. Dynamics of the interplanetary gas and magnetic fields. *Astrophys. J.*, 128:664–676, 1958.

[27] G. D Racca. Capability of solar electric propulsion for planetary missions. *Planetary and Space Science*, 49:1437–1444, 2001.

[28] M. D. Rayman, P. Varghese, D. H. Lehman, and L. L. Livesay. Results from the deep space 1 technology validation mission. *Acta Astronautica*, 47, 2000.

[29] D. V. Sivukhin. *Reviews of Plasma Physics*, volume 1. New York Consultants Bureau, 1965.

[30] J. P. Squire, F. R. Chang-Díaz, T. W. Glover, V. T. Jacobson, D. G. Chavers, R. D. Bengtson, E. A. Bering, R. W. Boswell, R. H. Goulding, and M. Light. Progress in experimental research of the VASIMR engine. *Fusion Sci. and Tech.*, 43:111–117, 2003.

[31] R. A. Stern and J. A. Johnson. Plasma ion diagnostics using resonant fluorescence. *Phys. Rev. Lett.*, 34(25):1548–1551, Jun 1975.

[32] M. Tanaka and I. Kimura. Current distribution and plasma acceleration in mpd arcjets with applied magnetic fields. *J. Propul. Power*, 4:428, 1988.

[33] S. Brophy J. Tikhonov, V. Semenikhin and J. Polk. Performance of 130 kw mpd thruster with an external magnetic field and li as propellant. *International Electric Propulsion Conference*, pages 197–117, 1997.

[34] K. Toki, S. Shinohara, T. Tanikawa, and K.P. Shamrai. Small helicon plasma source for electric propulsion. *Thin Solid Films*, 506-507:597–600, 2006.

[35] K. Tucek, J. Carlsson, and H. Wider. Comparison of sodium and lead-cooled fast reactors regarding reactor physics aspects, severe safety and economical issues. *Nucl. Eng and Design*, 236:1589, 2006.

[36] J. VonNeumann and R. D. Richtmyer. A method for the numerical calculation of hydrodynamic shocks. *Journal of Applied Physics*, 21(3):232–237, 1950.

[37] M. L. R. Walker, R. R. Hofer, and A. D. Gallimore. The effects of nude faraday probe design and vacuum facility backpressure on the measured ion current density profile of hall thruster plumes. In *38th Joint Propulsion Conference, IN, July 7-10, 2002*, page 4253. AIAA, 2002.

[38] J. R. Wertz. *Space Mission Analysis and Design.* Microcosm Press, 1999.

[39] R.J. White and M. Averner. Humans in space. *Nature*, 409:1115–1118, 2001.

[40] C. Williams. Application of recommended design practices for conceptual nuclear fusion space propulsion systems. *AIAA 2004*, page 3534, 2004.

[41] K. Yee. Numerical solution of inital boundary value problems involving maxwell's equations in isotropic media. *IEEE Trans. Antennas Propag.*, 14:302, 1966.

[42] T. M. York, B. A. Jacoby, and P. Mikellides. Plasma flow processes within magnetic nozzle configurations. *J. Propul. Power*, 8:1023, 1992.

Index

Vita

Mikhail Tushentsov was born in Nizhny Novgorod (Gorky), Russia (USSR), 24 June 1977, the son of Zoya I. Tushentsova and Rostislav A. Tushentsov. He received the Bachelor of Science degree in Physics from the Nizhny Novgorod State University, Russia in 1998 and M.S. degree in 2000. From 1997 to 2001 he was employed by Institute of Applied Physics Russian Academy of Sciences as a Junior Research Scientist. From 1999 to 2002 he was a guest researcher in Chalmers University of Technology, Gothenburg, Sweden. Since 2004 he has been pursuing a Ph.D. degree in physics in the University of Texas at Austin. His research has concentrated on the area of the interaction of the electromagnetic radiation with matter and advanced propulsion concepts.

Permanent address: 12625 Monterey Path
Austin, Texas 78732

This dissertation was typeset with LaTeX[†] by the author.

[†] LaTeX is a document preparation system developed by Leslie Lamport as a special version of Donald Knuth's TeX Program.